The auditory cortex of bats has a better signal to noise ratio and lower inter-trial variability in response to stimuli trains than mice

Katrina E. Deane[1*], Francisco García-Rosales[2,3], Ruslan Klymentiev[1], Julio C. Hechavarria[2°], Max F. K. Happel[1,4,5°]

1) Leibniz Institute for Neurobiology, D-39118 Magdeburg, Germany^
2) Institute for Cell Biology and Neuroscience, Goethe-University, D-60323 Frankfurt/M, Germany^
3) Ernst Strüngmann Institute (ESI) for Neuroscience in Cooperation with Max Planck Society, D-60528 Frankfurt/M, Germany
4) Center for Behavioral Brain Sciences (CBBS), D-39106 Magdeburg, Germany
5) MSB Medical School Berlin, Medical Faculty, D-14197 Berlin, Germany

* Correspondence should be addressed to KED (katrina.deane@lin-magdeburg.de)

° Equal contribution of last authorship

^ Work conducted at 1 and 2

Abstract

The brains of black 6 mice (*Mus musculus*) and Seba's short-tailed bats (*Carollia perspicillata*) weigh roughly the same and share the mammalian neocortical laminar architecture. Bats have highly developed sonar calls and social communication and are an excellent neuroethological animal model for auditory research. Mice are olfactory and somatosensory specialists and are used frequently in auditory neuroscience, particularly for their advantage of standardization and genetic tools. Investigating their potentially different general auditory processing principles would advance our understanding of how the ecological needs of a species shape the development and function of the mammalian nervous system. We compared two existing datasets, recorded with linear multichannel electrodes down the depth of the primary auditory cortex (A1) while awake, across both species while presenting repetitive stimulus trains with different frequencies (~5 and ~40 Hz). We found that while there are similarities between cortical response profiles in bats and mice, there was a better signal to noise ratio in bats under these conditions, which allowed for a clearer following response to stimuli trains. This was most evident at higher frequency trains, where bats had stronger response amplitude suppression to consecutive stimuli. Phase coherence was far stronger in bats during stimulus response, indicating less phase variability in bats across individual trials. These results show that although both species share cortical laminar organization, there are structural differences in relative depth of layers. Better signal to noise ratio in bats could represent specialization for faster temporal processing shaped by their individual ecological niches.

Introduction

The brains and bodies of black 6 mice (*Mus musculus)* and Seba's short-tailed bats (*Carollia perspicillata)* weigh roughly the same. Bats make up the second largest extant mammalian order, *Chiroptera* (Greek for "hand-wings"), after rodents, *Rodentia*, and they are the only mammals that can achieve true flight—converging their evolution with birds. Instead of sharing brain architecture with other flyers, they share neocortical laminar structures and microcircuitry with the rest of mammals, such as mice and humans (Chang & Kawai, 2018; García-Rosales et al., 2019; Linden & Schreiner, 2003; Mountcastle, 1997). Bats have highly developed sonar calls and social communication (Beetz et al., 2017; Hechavarría, Macías, Vater, Mora, et al., 2013; Thies et al., 1998; Weineck et al., 2020), making them a choice target for neuroethological auditory studies. Mice have a smaller repertoire of social verbal cues (Fonseca et al., 2021) and rely most heavily on their whiskers and olfaction for navigation (Gire et al., 2016), but they are frequently used in auditory neuroscience due to standardization and a wide transgenic toolkit.

There are two primary motivations for an exploratory cross-species analysis of the primary auditory cortex. First, investigating the potentially different application of general auditory processing would help to gain a better understanding of how the ecological needs of a species shape the development and function of the nervous system. Second, studies of the A1 may list a variety of species in their literature review to exemplify peer-reviewed findings, such as about oscillatory activity (e.g. cortical gamma in **mouse**: Chen et al., 2017: Shahriari et al., 2016; in **rat**: MacDonald & Barth, 1995: Vianney-Rodrigues et al., 2011; in **cat**: Karmos et al., 2002; Lakatos et al., 2004; etc.) or cortical layer roles (e.g. in **bat**: García-Rosales et al., 2019; in **mouse**: Chang & Kawai, 2018; in **rabbit**: McMullen & Glaser, 1982; in **cat**: Winguth & Winer, 1986, in **primate** Hashikawa et al., 1995; etc.). However, the ecology and evolutionary biology of the model may lead to A1 discrepancies in a species-specific way that has not been previously quantifiable through comparing across publications nor, to the authors' knowledge, reviewed on a broad scale. While there are some studies comparing the A1 and dorsal auditory cortical areas of several bat species (e.g. Hagemann et al., 2011; Hechavarría et al., 2013), few compare the A1 of bats to other mammals (see Kanwal & Rauschecker, 2007). Similarly, there are few studies quantitatively comparing the mouse A1 against other species (see Hoglen et al., 2018).

In this paper, we investigated the A1 of awake, head-fixed, freely moving black 6 mice and awake, head-fixed Seba's short-tailed bats. We evaluated two existing A1 multichannel datasets of local field potential (LFP) recordings across both species to perform comparative analyses aimed at understanding fundamental auditory response profiles between them. Bats listened to a repeated distress syllable at 5.28 and 36.76 Hz and mice listened to click trains at 5 and 40 Hz. We explored laminar profiles with current source density (CSD) analysis. We performed a model fit analysis to better understand temporal response and background suppression over consecutively repeated stimuli trains across these two data sets. We further ran continuous wavelet transform (CWT) analysis to compare internal coherence dynamics and signal to noise ratio differences. We also computed phase amplitude coupling (PAC) over the LFP and CSD to investigate remote and local contributions to information transfer and spectral coupling profiles.

Overall, we found that the laminar flow of cortical activity in response to stimuli was highly conserved across short-tailed bats and mice. However, bats demonstrated a better signal to noise ratio under these conditions, via more robust stimulus-related activity, and more accurate temporal resolution in response to stimuli trains. CWT analysis revealed a stronger broadband oscillatory frequency power distribution during stimulus response, relative to the background, and stronger phase coherence during stimulus response in bats. PAC profiles were fundamentally different between species. These results provide meaningful insight into the divergent recruitment of shared mammalian auditory physiology, linking evolutionary and behavioral need to specific auditory ability.

Methods

Ethical Approval

All experiments were conducted in accordance with ethical animal research standards defined by the German Law and approved by an ethics committee of the State of Saxony-Anhalt under the given license 42502-2-1394LIN for mice and by the Darmstadt Regional Counsel under the given license #FU-1126 for bats. They also conform to the principles and regulations as described in by Grundy (Grundy, 2015). All experiments were carried out with adult male mice (*Mus musculus*, n = 2, 6-13 weeks of age, 20-28 g body weight) and adult Seba's short-tailed bats (*Carollia perspicillata*, n = 5, 18-20 g body weight). Note that female mice were not

used as possible variances due to sex was not in the scope of our study.

Pharmacology

For mice, pentobarbital (Nembutal, H. Lundbeck A/S, Valby, Denmark) was administered at the onset of surgery with an intraperitoneal infusion of 50 mg per 1 kg of bodyweight and supplemented by 20% every hour. Anesthetic status was regularly checked (every 10-15 min) by paw withdrawal reflex, tail pinch, and breathing frequency. Body temperature was kept stable at 37°C.

Mice received analgesic treatment with Metacam substituted by 5% glucose solution 30 minutes before the end of surgery with 0.3 ml per 1 kg of bodyweight and for 2 days post-operatively with 0.2 ml per 1 kg of bodyweight.

For bats, ketamine-xylazine was administered at surgery onset (ketamine: Ketavet, 10 mg/kg, Pfizer; xylazine: 38 mg/kg). For surgery, and for any subsequent handling of the wounds, a local anesthetic (ropivacaine hydrochloride, 2 mg/ml, Fresenius Kabi, Germany) was applied in the scalp area.

Surgery and probe implantation

For mice, the right auditory cortex was exposed by trepanation and the A1 was located by vascular landmarks. A small hole was drilled on the contralateral hemisphere, over the visual cortex, for implanting a stainless-steel reference wire (Ø 200µm). A recording electrode with a flexible bundle between shaft and connector (A1x32-6mm-50-177_H32_21mm, Neuronexus, Ann Arbor, Michigan USA) was inserted perpendicularly in the A1 and secured with UV-curing glue (Plurafill flow, Pluradent GmbH & Co. KG Magdeburg, Germany). To protect the exposed region of the cortex, the hole was filled with a small drop of an artificial dura replacement compound (Dura-gel, Cambridge Neuro-Tech, Cambridge UK) before being encapsulated. A 3D printed headplate was secured to the top of the exposed skull with dental cement (Paladur, Heraeus Kulzer GmbH, Germany) and the connector (H32-omnetics, Neuronexus) was glued to the top of this headplate with a UV-curing glue and dental cement. Animals were allowed to recover for at least 3 days before habituation to their head-fixation setup.

For bats, the surgical procedure is described in (García-Rosales et al., 2020). Briefly, A1s were exposed through craniotomy (ca. 1 mm^2) performed with a scalpel blade. The animals were allowed to recover for at least two days before recording. A head post (1 cm length, 0.1 cm diameter) was cemented on the skull with dental cement (Paladur) for fixation.

Electrophysiological recordings

Mice were placed on a head-fixation treadmill (designed in lab) for 5 days of habituation (from 15 to 75 minutes head-fixed). This treadmill was in a Faraday-shielded acoustic soundproof chamber with a speaker (Tannoy arena satellite KI-8710-32, Tannoy Germany) located 1 m from the head-fixation platform. Recorded local field potentials (LFPs) were fed via an Omnetics connector (HST/32V-G2O LN 5V, 20x gain, Plexon Inc., Dallas, Texas USA) into a PBX2 preamplifier (Plexon Inc.) to be pre-amplified 500-fold and band-pass filtered (0.7-300 Hz). Data were then digitized at a sampling frequency of 1000 Hz with the Multichannel Acquisition Processor (Plexon Inc.). After habituation, mice were head-fixed on the treadmill for 7 consecutive days to record cortical responses to click trains (stimuli duration: 999 ms; click presentation frequency: 5 and 40 Hz; inter-stimulus-interval: 200 and 25 ms respectively; inter-trial-interval: 3 s; carrier tone: pre-determined auditory best frequency; 50 pseudorandomized repetitions; 90 dB sound pressure level; 15 min per measurement) and spontaneous activity (~2 min; no stimuli while recording brain activity from this area). Stimuli in this setup were generated in Matlab (Mathworks, R2006b), converted into analog (sampling frequency 1000 Hz, NI PCI-BNC2110, National Instruments), routed through an attenuator (g-PAH Guger Technologies, Graz, Austria), and amplified (Thomas Tech Amp75, Tom-technology, Ilirska Bistrica, Ljubljana). A microphone and conditioning amplifier were used to calibrate acoustic stimuli (G.R.A.S. 26AM and B&K Nexus 2690-A, Brüel&Kjær, Naerum, Denmark). Each subject had 2 click-train measurements per day, totaling 28 for the group, and 2-3 spontaneous measurements per day, totaling 35 for the group.

Bats were placed in a custom-made holder in a Faraday sound-proof chamber and kept at a constant body temperature of 30°C with a heating blanket (Harvard, Homeothermic blanket control unit). A speaker (NeoCD 1.0 Ribbon Tweeter; Fountek Electronics, Hong Kong, China) was positioned 12 cm away from the bat's right ear. Recordings were made in the left A1. Per recording session, a laminar probe (A1x16-50-177, NeuroNexus) was inserted perpendicularly into the A1 until the uppermost channel was barely visible at the cortical surface. The probe was connected to a micro preamplifier (MPA 16, Multichannel Systems MCS GmbH, Reutlingen, Germany), connected to an integrated amplifier and analog-to-digital converter with 32-channel capacity (model ME32 System, Multi Channel Systems MCS GmbH). Acoustic stimulation, delivered by Matlab (R2009b), were trains of a single

distress syllable (representative of this bat's distress repertoire; stimuli duration: 2 s; click presentation frequency: 5.28 or 36.76 Hz; inter-stimulus-interval: 189.39 and 27.02 ms respectively; inter-trial-interval: 1 s; 50 pseudorandomized repetitions; intensity: 70 dB SPL rms). Auditory stimuli were digital-to-analog converted using a sound card (M2Tech Hi-face DAC, Pisa Italy, 32 bit; sampling frequency: 192 kHz) and amplified (Rotel power amplifier, model RB-1050, Rotel Europe, West Sussex, England). Spontaneous activity was also recorded at the beginning of each session for 2+ minutes. Bats were used a varying number of times, ranging from 5 to 14 recording sessions. From 5 bats, there was a total of 46 probe penetrations/measurements.

Current Source Density Analysis

Based on the recorded laminar local field potentials, the second spatial derivative was calculated in Matlab (R2016a-R2022a), yielding the CSD distribution as seen in equation 1:

$$\mathrm{CSD} \approx \frac{\delta^2 \Phi(z)}{\delta z^2} = \frac{\Phi(z+n\Delta z) - 2\Phi(z) + \Phi(z-n\Delta z)}{(n\Delta z)^2} \quad (1)$$

where Φ is the field potential, z is the spatial coordinate perpendicular to the cortical laminae, Δz is the sampling interval, and n is the differential grid (Mitzdorf, 1985). LFP profiles were smoothed with a weighted average (Hamming window) of 9 channels which corresponds to a spatial kernel filter of 450 µm (Happel et al., 2010). CSD distributions reflect the local spatiotemporal current flow of positive ions from extracellular to intracellular space evoked by synaptic populations in laminar neuronal structures. Current sinks thereby correspond to the activity of excitatory synaptic populations, while current sources mainly reflect balancing return currents. Early synaptic thalamocortical inputs persist after intracortical silencing with the $GABA_A$-agonist muscimol related to thalamocortical projections on cortical layers III/IV and Vb/VIa (Brunk et al., 2019; Deane et al., 2020; Happel et al., 2010, 2014; Happel & Ohl, 2017) in accordance with reports by others (Schaefer et al., 2015). Early current sinks in the auditory cortex are therefore indicative of thalamic input in granular layers III/IV and infragranular layers Vb/VIa (Happel et al., 2010; Szymanski et al., 2009).

CSD profiles were further transformed by averaging the rectified waveforms of each channel by equation 2:

$$AVREC = \frac{\sum_{i=1}^{n} |CSD_i|(t)}{n} \quad (2)$$

where n is the individual channel and t is time in ms. This measure gives us the overall temporal local current flow of the columnar activity (Givre et al., 1994; Schroeder et al., 1998).

Model Fit Analysis

A model fit analysis was performed on the averaged peak amplitudes after peak detection on measurement-averaged traces. Peak detection was calculated with the *max* function in Matlab within detection windows after each stimulus in a presented stimulus train (e.g. for 5 Hz click stimulus, 5 peaks were detected—1 peak after each click). For each of the AVREC and layer trace peak amplitude datasets, 2 models were fitted: exponential decay seen in equation 3 and linear regression seen in equation 4.

$$Exponential\ Decay = ae^{-b\,O} + c \quad (3)$$

where $a + c$ is the intercept (the first observed peak amplitude), meaning a is depth or the distance between the first observed amplitude and c, b is the rate of decay (the greater the value, the steeper the decay), c is the offset (the value at which the model attenuates), and O is the order of peak amplitudes.

$$\boldsymbol{Linear\ Regression = b_0 + b_1 O} \quad (4)$$

where b_0 is the intercept, b_1 is the slope, and O is the order of peak amplitudes. We used the function *minimize* from the Python SciPy package (Virtanen et al., 2020) to estimate the model parameters. The function used Broyden-Fletcher-Goldfarb-Shanno algorithm to minimize the root mean square error (RMSE), in equation 5:

$$\mathbf{RMSE} = \sqrt{\frac{\sum_{i=1}^{N}(y_i - \hat{y}_i)^2}{N}} \quad (5)$$

where y_i is the actual value, $\hat{y}_i$ is the estimated value by the model, and N is the number of data points. Model fits and detected peaks were then plotted with overlaid model parameters and RMSE value. Note that indexing in python meant the models started at index 0 but plotting starts at value 1 call or click.

Phase Amplitude Coupling Analysis

Phase amplitude coupling (PAC) was calculated for each stimulus frequency and on spontaneous activity per measurement, based on methodology by Kikuchi et al. (2017) and García-Rosales et al. (2020). LFP signals were filtered in the following low frequency bands with a 4th order bandpass Butterworth filter (Matlab function *filtfilt*): 1 to 3, 3 to 5, … 13 to 15 Hz. LFP signals were also filtered in the following high frequency bands: 25 to

35, 30 to 40, … 95 to 105 Hz. Hilbert transform was applied during the time window of stimulus presentation and, in the stimulus conditions, the average of across trials for the current stimulus and measurement was subtracted from the individual response of each trial to reduce the effect of stimulus-evoked cortical response. Instantaneous phase [φ (t)] for low frequencies and amplitude [A(t)] for high frequencies was then extracted.

To minimize the effect of phase non-uniformities (clustering) in the signal caused by non-oscillatory periodicities in the field potentials, the mean vector of the phase angles was linearly subtracted from the instantaneous phase time series with equation 6:

$$\phi'(t) = e^{i\phi(t)} - \frac{1}{n}\sum e^{i\phi(t)} \quad (6)$$

where □^′ *(t)* denotes the corrected (de-biased) phase at time t, and n represents the number of series time points. With □^′*(t)* and *A(t)*, a composite time series *z(t)=A(t)* × □^′ *(t)* was constructed. From *z(t)*, the modulation index (MI) was quantified with the following equation 7:

$$MI = \left|\frac{1}{n}\sum z(t)\right| \quad (7)$$

PAC is susceptible to a number of biases in how it is calculated and on the structure of the input signal. A direct comparison between species resulted in very different MI scores across PAC calculations at different frequency pairings. We therefore also computed a surrogate MI by matching the phase series of a given trial with amplitude series of another trial and recalculating surrogate MIs (n = 500) to create a distribution against which we compared observed MI scores (see García-Rosales et al., 2020 Figure 3a). Observed MI scores were z-normalized to the surrogate distribution to obtain the z-scored MI (zMI). If no effect of PAC existed in the data, zMI values would hover around 0, whereas coupling effects would yield zMIs significantly higher than 0 (z-score > 2.5). These zMI values were then arranged into a matrix of high frequency amplitude over low frequency phase PAC pairings and these matrices were used for measurement-normalized comparisons between species over cortical layers. Regions of interest (ROI) were determined based on each species strongest area of PAC, and a clustermass permutation analysis was run on both ROIs per comparison (see below).

The clustermass permutation analysis is specifically suited to control for a familywise error rate (FWER; cf. Groppe et al., 2011). We extracted a *t* statistic pointwise across matrices in comparison of groups and pre-selected a significance *t* threshold based on a two-tailed p-value < 0.05. Any statistic result at or above this significance threshold was converted to a 1 and anything below was converted to a 0—creating a binary matrix of 0s and 1s, where 1 is a possible point of significance in the comparison of those matrices. The 1s within each ROI were then summed to create our observed clustermass values. Next, we permuted the groups 500 times; condition containers were created, equal to observed group sizes, and the matrices from both groups were combined and randomly allocated into those containers. The same point-wise statistic-and-threshold-calculated binary map was produced for each permutation with the total sum of 1s for each ROI taken as a permutation clustermass value. This created a distribution of 500 permutation clustermass values to which the observed clustermass could be compared. A p-value was calculated according to where the observed clustermass value fell onto the permutation distribution. This test indicates if the difference in the observed conditions is significant above chance—or put another way, it tells us how reliable the observed results are.

Continuous Wavelet Transform Analysis

Spectral analysis was performed in Matlab using the wavelet analysis toolbox function *CWT* (short for Continuous Wavelet Transform) for the following variables: animal, condition, stimulus, and recorded signal. Important parameters fed into the CWT were as follows: layer channels from CSD profiles, frequency limits: 5 to 100 Hz (below the Nyquist), and wavelet used: analytic Morse (Lilly & Olhede, 2012; Olhede & Walden, 2002). For layer-wise wavelet analysis, 3 channels centered on the middle channel of each layer were averaged and fed into the CWT. A trial-averaged scalogram was calculated for each cortical layer and wavelet power—per frequency, per time point—for each subject with equation 8.

$$\boldsymbol{Power} = |\boldsymbol{a} + \boldsymbol{b_i}|^2 \quad (8)$$

where $a + b_i$ represents the complex number output of the trial-averaged CWT analysis (Lachaux et al., 1999). Single trial scalograms were calculated for each animal as well and, on these, phase coherence—per frequency, per time point—for each subject was computed with equation 9:

$$\boldsymbol{Phase\ coherence} = \left|\frac{\sum^{(a+b_i)}/_{|a+b_i|}}{n}\right| \quad (9)$$

Power and phase coherence data were averaged pointwise (frequency and time bins were consistent across averages) for group plots. Clustermass

permutations (as above) were performed for the difference between spectral representations in each layer, with the ROI time limited to the onset of the stimuli train until before the second stimulus in the train. Frequency bands were split as follows: theta 4-7 Hz, alpha 8-12 Hz, low beta 13-18 Hz, high beta 19-30 Hz, low gamma 31-60 Hz, and high gamma 61-100 Hz. For power calculations: the test statistic for permutation was the student's t test and a Cohen's D matrix was generated to indicate effect size per frequency at each time point. For phase coherence calculations: the test statistic for permutation was the non-parametric Mann-Whitney-U (MWU; Cardillo, 2009; Maris et al., 2007) test and effect size, r, was indicated with the z score output as in equation 10:

$$r = \left| \frac{z}{\sqrt{n}} \right| \quad (10)$$

Results

Shared microcircuitry but differing cortical response profiles

Seba's short-tailed bats and black 6 mice have a similarly thick auditory cortex, but it is slightly more in mice (~1 mm; Chang & Kawai, 2018) than in bats (~750 µm; García-Rosales et al., 2019). Figure 1 shows the group averaged CSD profiles for bats and mice at ~5 and ~40 Hz stimulus presentation and Supp Figure 1 shows an anatomical comparison of the averaged group CSDs to the above references. Awake, head-fixed bats heard a species-specific distress call repeated at 5.28 and 36.76 Hz , over 2 seconds (1 second of stimulus presentation is shown here for comparison; see García-Rosales et al. 2020). Awake, head-fixed, freely moving mice were presented with click trains at 5 and 40 Hz over 1 second. Motivated by the overlapping recording technique (Neuronexus probes with 50 µm channel distance and 177 µm² channel diameter), we believe a comparison on basic functional circuitry differences is justified as an exploratory exercise to highlight possible differences and commonalities in cortical processing in bats vs. rodents (see discussion).

The supragranular layer at the penetration sites across the bat A1 was proportionally much thicker than that found across mice and had a very strong and consistent following response which lagged behind the thalamocortical response (Figure 1A; Supp Figure 1). In the awake mice average CSD profile (Figure 1B), the granular sink was very light in comparison to the early infragranular response. Where we saw very clear following responses down the depth of the cortex in bats at a lower (5.28 Hz) and higher (36.76 Hz) frequencies, the following response in mice was noisier and more relegated to thalamic input areas, with separate, repeated granular and infragranular sinks following the stimuli. The noisier signal seen in awake mice was not surprising in comparison with the classically less noisy ketamine-anesthetized signals in mice as well as Mongolian gerbils (Deane et al., 2020, 2022), due to ketamine being a neuronal synchronizer. Interestingly, the awake bat cortical activity was then less noisy compared to these awake rodent datasets (looking more similar to the anesthesia-induced synchrony in data cited above), in the sense of legible sinks far above the baseline cortical activity for each stimulus onset. The infragranular and granular sinks were smeared into one large cortical response sink in bats. However, that sink smearing might have been due to different penetration sites per experimental session (as opposed to a single chronically implanted penetration in mice). Therefore, layer selection was done on a per-penetration or per-measurement basis for all subsequent analysis.

Accurate cortical following responses through all layers in bats

Figure 2 shows the averaged Average Rectified CSD (AVREC) and layer traces per group for ~5 and ~40 Hz. Amplitude was normalized to each measurement's first AVREC peak detected in their 2 Hz conditions. This visually represents the relative contribution of the layers to the full cortical column activity.

Sinks originating in the granular layer of mice often spread up into supragranular layers, causing a stimulus-locked, small amplitude response at tone onset and following the lower frequency click trains (Figure 1). In the bats, the supragranular layer consistently lagged the stimulus-locked thalamic input activity of layers III/IV, V, and VI, creating an accurate, yet lagged, following response to low and high frequency stimulus presentations. Not only did this confirm what was visible in the CSD profiles, that the stimulus following response was clearly visible through the depth of the bat A1, but also that it builds concisely to the AVREC. In both bat and mouse ~5 Hz AVREC traces, there was an initial onset response in the full column and a second, smaller and broader peak after both the first and second stimulus responses. In the bats, that broader peak was driven almost exclusively by the supragranular activity. In the mice, a second, broader peak was seen in all layers, creating less laminar specificity and causing the AVREC to build the second peak of activity from throughout the column.

Mouse cortical activity was also noisier than bat cortical activity. While bat averaged traces revealed almost

uniform following responses at high and low stimulus presentation frequencies, mouse cortical activity seemed to contain more high frequency jitter and more variable following response profiles across consecutive stimuli presentation (see quantitative analysis of this in both the model fit and continuous wavelet analysis below). Following responses at 40 Hz in mice were visible in independent layers, especially layer III/IV, but not as clearly visible in the AVREC compared to bat following responses at 36.76 Hz. In mice, layer V was where the onset signal was strongest. In bat layers IV and V, the onset response and following response was more equivalent. However, layer I/II in bats at 36.76 Hz had the highest amplitude consecutive following response compared to the AVREC and other layers. Here also, there was a slow wave buildup of activity over the first 200 ms which then subsided by 500 ms and remained fairly consistent in amplitude afterwards. The base level of activity in mice during stimuli presentation stayed higher, potentially in part due to the noisiness of the trace. This was clearest in the supragranular layer but also seen through the layers and in the AVREC after stimuli onset. Activity in bats, in comparison, began closer to relative 0 (as this is normalized to the peak of the AVREC at 2 Hz) and then sank back to near 0 in each layer after the onset response. The only exception was in the first 500 ms of the supragranular activity where there was the slow wave build-up, and in the AVREC trace which included both sink and source activity rectified.

Because we could see the following response riding the onset response in the bats at 36.76 Hz, we separated these two components with bandpass filters (Supp Figure 2). We filtered +/- 3 Hz around the stimulus frequency to reveal, more strictly, the following response components and we filtered from 1 to 4 Hz to reveal the onset response. With the stimulus frequency filter, bats layer I/II showed the same response lag and then a consistent amplitude following response. In each of the granular and infragranular layers, there was a relatively consistent higher amplitude following response in the first ~100 ms of tone presentation which then attenuated to a more even following response to consecutive stimuli. In mice at 40 Hz, the following response was more variable throughout the layers. Attenuation to consecutive responses was also more variable in mice. With the onset component filter, the onset in bats was consistently higher than mice in the AVREC, granular, and infragranular layer traces. The supragranular layer was nearly flat in bats but the previously described, lagged, slow wave was visible in both species with this filter. In mouse layer V, especially, there was a double-peak wave, indicating non-onset related slow-wave activity.

A greater dynamic range in response amplitude to consecutive stimuli in bats

To characterize the response profile across consecutive stimuli presentations at a low (~5 Hz) or high (~40 Hz) frequencies, we performed a model fit analysis, with 2 models to choose from algorithmically: exponential or linear. Figure 3 shows the averaged peak amplitudes of responses after stimuli overlaid with the model selected and its fit value (root mean square error, RMSE) and parameters. The best fitting model was typically exponential decay. For bats, at both presentation frequencies, exponential decay was selected in all traces except the supragranular layer at 36.76 Hz, where a linear fit was selected. At 5 Hz in mice, layer III/IV and V were the only traces selected for exponential decay. In these layers, the exponential fit was a better choice for the bat dataset. In mice, the offset of 5 Hz layer III/IV was well below a possible peak amplitude due to how shallow the rate of decay was, and the rate of decay in 5 Hz layer V was severely steep.

The bat 5.28 Hz III/IV and V models were comparable to each other and spanned a greater dynamic range (intercept – offset) than mouse 5 Hz V. In ~40 Hz, datapoints were more aligned with an exponential fit for bats in every case except the AVREC peak amplitudes. Importantly, bats had a greater dynamic range parameter in the AVREC and layers III/IV through VI, indicating again a consistently deeper suppression of consecutive responses at this higher frequency presentation. In the AVREC, layer III/IV, and V, mice adapted faster (with a steeper decay rate) to repeated stimulus and vice versa in layer VI.

To exclude that the onset component was the main effector for the model fitting, we ran the same analysis with bandpass-filtered signals (Supp Figure 3). The model fits between both species were more similar but they did not explain the data as well as when the onset response component was included. The bat data still generally showed a greater dynamic range than mice throughout the layers. This revealed that even without the large onset response component, cortical response to consecutive stimuli was more deeply suppressed in bats.

Better signal to noise ratio in spectral power scalograms and stronger phase coherence in bats

We performed CWT analysis to discern both inter-trial phase variability through the lens of phase coherence and signal to noise ratio through normalized spectral

power. After CWT was computed on the center 3 channels of each layer, power and phase coherence scalograms were extracted for the low and high stimulus frequency presentation conditions (power: Figure 4 and phase coherence: Figure 5). Power was normalized to the maximum power in each measurement to result in a relative power of signal to background noise and to account for the large species difference in scale (bats had stronger unnormalized power by a factor of 3, not shown). Phase coherence is already a normalized metric ranging from 0 to 1. Permutation clustermass was run on 200 ms of baseline activity and the time-period from the onset of the stimulus train to the point of onset of the second stimulus (e.g., 5 /5.28 Hz: -200 to 189 ms). Across both power (Figure 4) and phase coherence (Figure 5) at these time points for both stimulus conditions and across all spectral frequency bands, clustermass was significantly higher than chance according to permutation analysis. This attested to a reliability in the observed results.

In comparisons of normalized spectral power (Figure 4), the background around stimulus response was significantly different, with mice showing a higher level of spectral noise relative to signal response. The time at which thalamic input reached the cortex (~15 ms), the cortical response had significantly higher power in bats for each signal response in the beta and low gamma range in the ~5 Hz condition and for the onset signal response in the theta through low gamma range in the ~40 Hz condition. A band of non-significant tests (with insignificant effect sizes) surrounded the higher spectral power of signal or onset response in bats to transition to the higher spectral power of the background in mice.

Phase coherence (Figure 5) was significantly stronger in bats across a broad band of spectral frequencies following each stimulus presentation in the ~5 Hz condition and at the onset signal response in the ~40 Hz condition. In this higher frequency condition, there was also a phase coherence around the stimulus presentation in the low gamma range which was significantly stronger in bats.

Fundamentally different local and global phase amplitude coupling profiles

Low oscillation phase coupled to high oscillation amplitude has been implicated in information transfer across neural tissue (Bonnefond et al., 2017; Gourévitch et al., 2020) and phase amplitude coupling (PAC) analysis is an increasingly common tool for exploring a range of possible coupling pairs. Here we performed PAC analysis within cortical layers of both species to differentiate coupling profiles. This analysis was done on low and high stimulus presentation frequencies on CSD signals (Figure 6) to distinguish local network PAC contributions.

PAC was strongest in mice centered around delta and high gamma pairings when present and strongest in bats around theta/alpha and low gamma pairings. These were chosen as ROIs for comparison between PAC profiles. Due to spatial distinction in the CSD signal, laminar differences were found in both species, with less or essentially no coupling in supragranular layers and more in the granular layer. Mouse layer III/IV through VI profiles revealed theta gamma (low and high) coupling at roughly equivalent levels in both high and low stimulus frequency conditions (see the difference in average PAC values overlaid on PAC profiles). The bat PAC was stronger during the 5.28 Hz condition compared to the 36.76 Hz condition, possibly indicating a stimulus dependance in bats. However, Bat PAC was only stronger than mouse PAC in layer III/IV in the ~5 Hz stimulus presentation. Generally, mouse PAC in the delta high gamma pairing was significantly higher after clustermass permutation testing.

PAC analysis was performed also on spontaneous, or resting state, activity (Figure 7). Several studies have found coupling that may assist remote activity across neuronal assemblies in the absence of a current stimuli to process (Wang et al., 2012; Weaver et al., 2016) which may explain the far stronger PAC in bats but does not explain the weak PAC in mice. During spontaneous activity, bats had PAC at a wider range of low frequencies phases and high frequencies amplitudes than in stimulus conditions. Bats had significantly higher PAC in both ROIs here. There were areas of large and huge effect sizes at delta/theta/alpha low gamma where the higher PAC in bats was centered.

Discussion

We compared the cortical response profiles across all layers of A1 in two small mammalian species, one a flying auditory specialist and one a land-based olfactory specialist. The nervous systems of both species have been adapted to fill specific ecological niches. Seba's short-tailed bats have sophisticated social communication and echolocate for navigation (Beetz et al., 2017; García-Rosales et al., 2022; Hechavarría et al., 2013; López-Jury et al., 2021; Thies et al., 1998; Weineck et al., 2020), meaning that temporally accurate perception of auditory signals is paramount to successful social and flying behavior. Mice have a smaller repertoire of social vocal cues (Fonseca et al., 2021) and rely on their whiskers and olfaction for navigation (Gire

et al., 2016), indicating that comparably precise cortical representation of auditory cues is not necessary for behavioral success. Our datasets were acquired with common recording equipment, although mice listened to a repeated artificial click and bats listened to a repeated, broadband, species-specific distress syllable. Through this novel comparison of CSD profiles, we have shown that, in these conditions, Seba's short-tailed bats have a better signal to noise ratio in auditory response to repetitive stimuli, unique PAC profiles, and less inter-trial phase variability than black 6 mice. We posit that these phenomena are based on a species-specific overall recruitment of the shared and conserved cortical canonical microcircuitry.

Shared mammalian laminar structure

While the laminar structure of the neocortex is shared between mammals (Mountcastle, 1997), there were some differences between Seba's short-tailed bat and black 6 mouse primary auditory cortex layers. The supragranular layer of activity revealed by CSD analysis (Figure 1) in bats was consistently thicker—taking up more channels on the probe relative to the full profile—than in mice. The distinction between supragranular and granular activity was clear in the bat CSD profiles, where the former had a definite lag behind the latter, but was less divergent in mouse CSD profiles. In histological studies of each's laminar profiles, layer I was proportionally thicker in the bat A1 (García-Rosales et al., 2019) than in mice (Chang & Kawai, 2018). While this agrees with the population activity we observed in this study, it did not fully account for how much deeper the uppermost sink activity protruded in the cortical depth. This may indicate differing recruitment of layer II neurons to either assist in layer I cross-columnar activity or in the layer III and IV excitation feedback circuitry between species. In the thinner bat A1 cortex, thalamic input to granular and infragranular layers appeared as more of a single sink. In the mouse A1, there were separable input sinks at the onset of a stimulus and both layer V and VI were thicker than in the bat CSD profiles. We found confirmation of these layer designations again from Chang & Kawai, (2018) and García-Rosales et al., (2019). Therefore, despite shared architecture, there were differences in the proportional layer sizes which likely contributed to the differing recruitment profiles across species.

A better signal to noise ratio in bats leads to lower resource cost on accurate stimuli representation

The bat auditory cortex may have been more readily primed for accurate processing due to the higher signal to noise ratio. This corresponds with findings showing forward suppression to sharpen cortical response and reduce spike rate per echo in echolocating bats (Macias et al., 2022). In the comparison of signal traces at ~5 and ~40 Hz (Figure 2), bat normalized cortical activity had less jitter around stimulus response. That is, the pre-stimulus baseline was closer to its relative 0 and cortical activity adapted back closer to relative 0 after onset and following responses. Mouse normalized activity was more variable. In the ~40 Hz condition of the model fit analysis (Figure 3) bats had a higher intercept (first observed peak amplitude) in the AVREC and thalamic input layers. They subsequently had a deeper suppression of response amplitude to consecutive responses, reflected in the higher dynamic range parameter. Due to the deeper suppression in bats, the response amplitude generally adapted slower to stimuli in these traces at ~40 Hz, reflected in the lower rate of decay parameter in the AVREC and layer V. Mice had a weaker onset response and a shallower rate of suppression to consecutive responses due to higher noise in the signal trace.

Further evidence was provided by the normalized power scalograms from the CWT analysis (Figure 4). The bat spectral power was significantly stronger at the timepoint of stimulus onset response throughout the layers. However, the background spectral power was significantly stronger in mice, especially at higher oscillation frequencies where stimulus response was at a shorter time scale. This suggests that signal to noise ratio was significantly better in bats, which may have created a cortical environment where stimulus processing is more temporally precise at a relatively lower activity cost to the neural populations.

Phase coherence revealed lower inter-trial variability in bat auditory response profiles

The phase coherence scalograms from CWT analysis revealed a significantly stronger inter-trial broadband phase coherence at the time of stimulus and following response (Figure 5). We had expected mice to have better coherence, the probes being chronically implanted in one site rather than moving around the penetration site per measurement (as in the bat dataset). Counterintuitively, the mouse data had consistently greater variability. This was notable in the level of background jitter in the AVREC and layer traces in mice and that their higher frequency stimulus presentation peak amplitudes were less aligned with the exponential model fits compared to bats.

Using two independent data sets for comparison innately bears the challenge to handle variability introduced by different stress levels between both species based on head-fixation techniques, session lengths, or the differences of the stimulus class, which may affect our physiological results. However, bat specialization in auditory perception also likely contributes to the significant discrepancies in the described cortical response variability. Bats require temporal precision in their echolocation and communication calls for behavioral success. That a bat has more accurate and less variable auditory responses to consecutive stimuli than a mouse, is evidence of successful specialization of shared architecture for different behaviors. Our analysis approach may foster further cross-species comparisons that could give us insight into the differential ways the mammalian cortex introduces or limits variability in populations of neurons based on ecological need.

Phase amplitude coupling fundamentally different between species

PAC is a well-established phenomenon throughout the brain and neocortex (Esghaei et al., 2015; Helfrich & Knight, 2016; Lisman & Jensen, 2013; O'Connell et al., 2015; Sotero et al., 2015; Spaak et al., 2012; Xiao et al., 2019), and has been implicated in a variety of relevant functional tasks such as interareal communication and information binding (Colgin et al., 2009; Daume et al., 2017). The functional use of PAC for information binding or the segmentation of continuous stimuli into slower times-scales of perceptual units, may be conserved through evolution as a shared mechanism in mammals (Garcia-Rosales et al., 2020). For example, in humans, theta gamma PAC has been implicated in efficient processing of speech phenomes into words and sentences (Gross et al., 2013; Lizarazu et al., 2019; Zion Golumbic et al., 2013). García-Rosales et al. suggested that bats could utilize this parsing strategy on echolocation to make sense of their auditory, and therefore spatial, scene. We ran a PAC coupling analysis on the A1 datasets for bats and mice at low and high stimulus presentation conditions and during spontaneous activity.

PAC in mice was similar in both stimulation frequencies, strongest in layer III/IV, but weakest during spontaneous activity. Coupling therefore seemed to depend on a stimulus being present but was not sensitive to the frequency of presentation (Figure 6 & 7). By contrast, bat PAC was different for low and high frequency stimuli and for spontaneous activity. Especially in layer III/IV, PAC was stronger at 5.28 Hz and strongest during spontaneous activity, indicating a stimulus dependent coupling strength.

Bats and mice were most different in their spontaneous activity PAC, where bats had a significantly stronger and broader area of coupling. Regardless of signal frequency, or whether it was stimulus derived or during resting-state, coupling was centered around delta/high gamma in mice and theta/low gamma in bats. The similarity in the bat PAC with human speech perception theta gamma coupling may support the hypothesized auditory scene parsing. However, this region may have had greater local A1 coupling because the stimuli was specifically a bat vocalization syllable. It is also possible that the delta/high gamma coupling in mice supports the same task in a different temporal scale.

Conclusion

When comparing two fundamentally different species, with alien subjective experiences, an analysis like this cannot say more than that these species have different interpretations of objective, external sound waves (Nagel, 1974). Nevertheless, cross-species comparisons can serve as valuable framework in consideration of shared, convergent, and divergent evolutionary adaptation (Sherry, 2007). Seba's short-tailed bats have adapted to an ecological niche which requires accurate temporal auditory perception during 3-dimensional navigation in flight and complex social communication. For mice accurate sound representation is less fundamental to find behavioral success in their environment. We have found that the neuronal signature of the auditory cortex in bats shows a significantly better signal to noise ratio, more accurate and less variable following responses to consecutive stimuli, far higher inter-trial phase coherence, and fundamentally different PAC profiles compared to mice. These discrepancies do not stem from differing cortical architecture, though some variance has been noted there, but from the divergent recruitment of the shared microcircuitry and laminar organization seen in all mammalian species.

References

Beetz, M. J., Kordes, S., García-Rosales, F., Kössl, M., & Hechavarría, J. C. (2017). Processing of Natural Echolocation Sequences in the Inferior Colliculus of Seba's Fruit Eating Bat, Carollia perspicillata. *ENeuro*, *4*(6), ENEURO.0314-17.2017. https://doi.org/10.1523/ENEURO.0314-17.2017

Bonnefond, M., Kastner, S., & Jensen, O. (2017). Communication between Brain Areas Based on Nested Oscillations. *ENeuro*, *4*(2), ENEURO.0153-16.2017. https://doi.org/10.1523/ENEURO.0153-16.2017

Brunk, M. G. K., Deane, K. E., Kisse, M., Deliano, M., Vieweg, S., Ohl, F. W., Lippert, M. T., & Happel, M. F. K. (2019). Optogenetic stimulation of the VTA modulates a frequency-specific gain of thalamocortical inputs in infragranular layers of the auditory cortex. *Scientific Reports*, *9*(1), 20385. https://doi.org/10.1038/s41598-019-56926-6

Cardillo, G. (2009). *MWWTEST: Mann-Whitney-Wilcoxon non parametric test for two unpaired samples.* http://www.mathworks.com/matlabcentral/fileexchange/25830

Chang, M., & Kawai, H. D. (2018). A characterization of laminar architecture in mouse primary auditory cortex. *Brain Structure and Function*, *223*(9), 4187–4209. https://doi.org/10.1007/s00429-018-1744-8

Chen, G., Zhang, Y., Li, X., Zhao, X., Ye, Q., Lin, Y., Tao, H. W., Rasch, M. J., & Zhang, X. (2017). Distinct Inhibitory Circuits Orchestrate Cortical beta and gamma Band Oscillations. *Neuron*, *96*(6), 1403-1418.e6. https://doi.org/10.1016/j.neuron.2017.11.033

Colgin, L. L., Denninger, T., Fyhn, M., Hafting, T., Bonnevie, T., Jensen, O., Moser, M.-B., & Moser, E. I. (2009). Frequency of gamma oscillations routes flow of information in the hippocampus. *Nature*, *462*(7271), Article 7271. https://doi.org/10.1038/nature08573

Daume, J., Gruber, T., Engel, A. K., & Friese, U. (2017). Phase-Amplitude Coupling and Long-Range Phase Synchronization Reveal Frontotemporal Interactions during Visual Working Memory. *Journal of Neuroscience*, *37*(2), 313–322. https://doi.org/10.1523/JNEUROSCI.2130-16.2016

Deane, K. E., Brunk, M. G. K., Curran, A. W., Zempeltzi, M. M., Ma, J., Lin, X., Abela, F., Aksit, S., Deliano, M., Ohl, F. W., & Happel, M. F. K. (2020). Ketamine anaesthesia induces gain enhancement via recurrent excitation in granular input layers of the auditory cortex. *Journal of Physiology*, *598*(13), 2741–2755. https://doi.org/10.1113/JP279705

Deane, K. E., Klymentiev, R., Heck, J., Mark, M. D., Ohl, F. W., Heine, M., & Happel, M. F. K. (2022). *Inhibiting presynaptic calcium channel mobility in the auditory cortex suppresses synchronized input processing* (p. 2022.03.30.486338). bioRxiv. https://doi.org/10.1101/2022.03.30.486338

Esghaei, M., Daliri, M. R., & Treue, S. (2015). Attention Decreases Phase-Amplitude Coupling, Enhancing Stimulus Discriminability in Cortical Area MT. *Frontiers in Neural Circuits*, *9*. https://www.frontiersin.org/article/10.3389/fncir.2015.00082

Fonseca, A. H., Santana, G. M., Bosque Ortiz, G. M., Bampi, S., & Dietrich, M. O. (2021). Analysis of ultrasonic vocalizations from mice using computer vision and machine learning. *ELife*, *10*, e59161. https://doi.org/10.7554/eLife.59161

García-Rosales, F., López-Jury, L., González-Palomares, E., Cabral-Calderín, Y., Kössl, M., & Hechavarria, J. C. (2020). Phase-amplitude coupling profiles differ in frontal and auditory cortices of bats. *European Journal of Neuroscience*, *n/a*(n/a). https://doi.org/10.1111/ejn.14986

García-Rosales, F., López-Jury, L., González-Palomares, E., Wetekam, J., Cabral-Calderín, Y., Kiai, A., Kössl, M., & Hechavarría, J. C. (2022). Echolocation-related reversal of information flow in a cortical vocalization network. *Nature Communications*, *13*(1), Article 1. https://doi.org/10.1038/s41467-022-31230-6

García-Rosales, F., Röhrig, D., Weineck, K., Röhm, M., Lin, Y.-H., Cabral-Calderin, Y., Kössl, M., & Hechavarria, J. C. (2019). Laminar specificity of oscillatory coherence in the auditory cortex. *Brain Structure and Function*, *224*(8), 2907–2924. https://doi.org/10.1007/s00429-019-01944-3

Gire, D. H., Kapoor, V., Arrighi-Allisan, A., Seminara, A., & Murthy, V. N. (2016). Mice develop efficient strategies for foraging and navigation using complex natural stimuli. *Current Biology : CB*, *26*(10), 1261–1273. https://doi.org/10.1016/j.cub.2016.03.040

Givre, S. J. J., Schroeder, C. E. E., & Arezzo, J. C. C. (1994). Contribution of extrastriate area V4 to the surface-recorded flash VEP in the awake macaque. *Vision Research*, *34*(4), 415–428. https://doi.org/10.1016/0042-6989(94)90156-2

Gourévitch, B., Martin, C., Postal, O., & Eggermont, J. J. (2020). Oscillations in the auditory system and their possible role. *Neuroscience and Biobehavioral Reviews*, *113*(April), 507–528. https://doi.org/10.1016/j.neubiorev.2020.03.030

Groppe, D. M., Urbach, T. P., & Kutas, M. (2011). Mass univariate analysis of event-related brain potentials/fields I: A critical tutorial review. In *Psychophysiology* (Vol. 48, Issue 12, pp. 1711–1725). Blackwell Publishing Inc. https://doi.org/10.1111/j.1469-8986.2011.01273.x

Gross, J., Hoogenboom, N., Thut, G., Schyns, P., Panzeri, S., Belin, P., & Garrod, S. (2013). Speech Rhythms and Multiplexed Oscillatory Sensory Coding in the Human Brain. *PLOS Biology*, *11*(12), e1001752. https://doi.org/10.1371/journal.pbio.1001752

Grundy, D. (2015). Principles and standards for reporting animal experiments in The Journal of Physiology and Experimental Physiology. In *Journal of Physiology* (Vol. 593, Issue 12, pp. 2547–2549). Blackwell Publishing Ltd. https://doi.org/10.1113/JP270818

Hagemann, C., Vater, M., & Kössl, M. (2011). Comparison of properties of cortical echo delay-tuning in the short-tailed fruit bat and the mustached bat. *Journal of Comparative Physiology A*, *197*(5), 605–613. https://doi.org/10.1007/s00359-010-0530-8

Happel, M. F. K., Deliano, M., Handschuh, J., & Ohl, F. W. (2014). Dopamine-Modulated Recurrent Corticoefferent Feedback in Primary Sensory Cortex Promotes Detection of Behaviorally Relevant Stimuli. *Journal of Neuroscience*, *34*(4), 1234–1247. https://doi.org/10.1523/JNEUROSCI.1990-13.2014

Happel, M. F. K., Jeschke, M., & Ohl, F. W. (2010). Spectral Integration in Primary Auditory Cortex Attributable to Temporally Precise Convergence of Thalamocortical

and Intracortical Input. *The Journal of Neuroscience*, *30*(33), 11114–11127.

Happel, M. F. K., & Ohl, F. W. (2017). Compensating Level-Dependent Frequency Representation in Auditory Cortex by Synaptic Integration of Corticocortical Input. *PLOS ONE*, *12*(1), e0169461. https://doi.org/10.1371/journal.pone.0169461

Hashikawa, T., Molinari, M., Rausell, E., & Jones, E. G. (1995). Patchy and laminar terminations of medial geniculate axons in monkey auditory cortex. *The Journal of Comparative Neurology*, *362*(2), 195–208. https://doi.org/10.1002/cne.903620204

Hechavarría, J. C., Macías, S., Vater, M., Mora, E. C., & Kössl, M. (2013). Evolution of neuronal mechanisms for echolocation: Specializations for target-range computation in bats of the genus Pteronotus. *The Journal of the Acoustical Society of America*, *133*(1), 570–578. https://doi.org/10.1121/1.4768794

Hechavarría, J. C., Macías, S., Vater, M., Voss, C., Mora, E. C., & Kössl, M. (2013). Blurry topography for precise target-distance computations in the auditory cortex of echolocating bats. *Nature Communications*, *4*, 2587. https://doi.org/10.1038/ncomms3587

Helfrich, R. F., & Knight, R. T. (2016). Oscillatory Dynamics of Prefrontal Cognitive Control. *Trends in Cognitive Sciences*, *20*(12), 916–930. https://doi.org/10.1016/j.tics.2016.09.007

Hoglen, N. E. G., Larimer, P., Phillips, E. A. K., Malone, B. J., & Hasenstaub, A. R. (2018). Amplitude modulation coding in awake mice and squirrel monkeys. *Journal of Neurophysiology*, *119*(5), 1753–1766. https://doi.org/10.1152/jn.00101.2017

Kanwal, J. S., & Rauschecker, J. P. (2007). Auditory cortex of bats and primates: Managing species-specific calls for social communication. *Frontiers in Bioscience : A Journal and Virtual Library*, *12*, 4621–4640.

Karmos, G., Lakatos, P., Pincze, Z., Rajkai, C., & Ulbert, I. (2002). Frequency of gamma activity is modulated by motivation in the auditory cortex of cat. *Acta Biologica Hungarica*, *53*(4), 473–483. https://doi.org/10.1556/ABiol.53.2002.4.8

Kikuchi, Y., Attaheri, A., Wilson, B., Rhone, A. E., Nourski, K. V., Gander, P. E., Kovach, C. K., Kawasaki, H., Griffiths, T. D., Howard, M. A., & Petkov, C. I. (2017). Sequence learning modulates neural responses and oscillatory coupling in human and monkey auditory cortex. *PLoS Biology*, *15*(4), e2000219. https://doi.org/10.1371/journal.pbio.2000219

Lachaux, J.-P., Rodriguez, E., Martinerie, J., & Varela, F. J. (1999). Measuring phase synchrony in brain signals. *Human Brain Mapping*, *8*(4), 194–208. https://doi.org/10.1002/(SICI)1097-0193(1999)8:4<194::AID-HBM4>3.0.CO;2-C

Lakatos, P., Szilágyi, N., Pincze, Z., Rajkai, C., Ulbert, I., & Karmos, G. (2004). Attention and arousal related modulation of spontaneous gamma-activity in the auditory cortex of the cat. *Brain Research. Cognitive Brain Research*, *19*(1), 1–9. https://doi.org/10.1016/j.cogbrainres.2003.10.023

Lilly, J. M., & Olhede, S. C. (2012). Generalized morse wavelets as a superfamily of analytic wavelets. *IEEE Transactions on Signal Processing*, *60*(11), 6036–6041. https://doi.org/10.1109/TSP.2012.2210890

Linden, J. F., & Schreiner, C. E. (2003). Columnar Transformations in Auditory Cortex? A Comparison to Visual and Somatosensory Cortices. *Cerebral Cortex*, *13*(1), 83–89. https://doi.org/10.1093/cercor/13.1.83

Lisman, J. E., & Jensen, O. (2013). The Theta-Gamma Neural Code. In *Neuron* (Vol. 77). https://doi.org/10.1016/j.neuron.2013.03.007

Lizarazu, M., Lallier, M., & Molinaro, N. (2019). Phase–amplitude coupling between theta and gamma oscillations adapts to speech rate. *Annals of the New York Academy of Sciences*, *1453*(1), 140–152. https://doi.org/10.1111/nyas.14099

López-Jury, L., García-Rosales, F., González-Palomares, E., Kössl, M., & Hechavarria, J. C. (2021). Acoustic Context Modulates Natural Sound Discrimination in Auditory Cortex through Frequency-Specific Adaptation. *Journal of Neuroscience*, *41*(50), 10261–10277. https://doi.org/10.1523/JNEUROSCI.0873-21.2021

MacDonald, K. D., & Barth, D. S. (1995). High frequency (gamma-band) oscillating potentials in rat somatosensory and auditory cortex. *Brain Research*, *694*(1–2), 1–12. https://doi.org/10.1016/0006-8993(95)00662-a

Macias, S., Bakshi, K., & Smotherman, M. (2022). Faster Repetition Rate Sharpens the Cortical Representation of Echo Streams in Echolocating Bats. *ENeuro*, *9*(1). https://doi.org/10.1523/ENEURO.0410-21.2021

Maris, E., Schoffelen, J.-M., & Fries, P. (2007). Nonparametric statistical testing of coherence differences. *Journal of Neuroscience Methods*, *163*(1), 161–175. https://doi.org/10.1016/j.jneumeth.2007.02.011

McMullen, N. T., & Glaser, E. M. (1982). Morphology and laminar distribution of nonpyramidal neurons in the auditory cortex of the rabbit. *The Journal of Comparative Neurology*, *208*(1), 85–106. https://doi.org/10.1002/cne.902080107

Mitzdorf, U. (1985). Current source-density method and application in cat cerebral cortex: Investigation of evoked potentials and EEG phenomena. *PHYSIOLOGICAL REVIEWS*, *65*, 64.

Mountcastle, V. B. (1997). The columnar organization of the neocortex. *Brain*, *120*(4), 701–722. https://doi.org/10.1093/brain/120.4.701

Nagel, T. (1974). What Is It Like to Be a Bat? *The Philosophical Review*, *83*(4), 435. https://doi.org/10.2307/2183914

O'Connell, M. N., Barczak, A., Ross, D., McGinnis, T., Schroeder, C. E., & Lakatos, P. (2015). Multi-Scale Entrainment of Coupled Neuronal Oscillations in Primary Auditory Cortex. *Frontiers in Human Neuroscience*, *9*. https://www.frontiersin.org/article/10.3389/fnhum.2015.00655

Olhede, S. C., & Walden, A. T. (2002). Generalized Morse wavelets. *IEEE Transactions on Signal Processing*,

50(11), 2661–2670. https://doi.org/10.1109/TSP.2002.804066

Schaefer, M. K., Hechavarría, J. C., & Kössl, M. (2015). Quantification of mid and late evoked sinks in laminar current source density profiles of columns in the primary auditory cortex. *Frontiers in Neural Circuits*, *9*, 1–16. https://doi.org/10.3389/fncir.2015.00052

Schroeder, C. E., Mehta, A. D., & Givre, S. J. (1998). A spatiotemporal profile of visual system activation revealed by current source density analysis in the awake macaque. *Cerebral Cortex*, *8*(7), 575–592. https://doi.org/10.1093/cercor/8.7.575

Shahriari, Y., Krusienski, D., Dadi, Y. S., Seo, M., Shin, H.-S., & Choi, J. H. (2016). Impaired auditory evoked potentials and oscillations in frontal and auditory cortex of a schizophrenia mouse model. *The World Journal of Biological Psychiatry: The Official Journal of the World Federation of Societies of Biological Psychiatry*, *17*(6), 439–448. https://doi.org/10.3109/15622975.2015.1112036

Sherry, D. F. (2007). Cross-Species Comparisons. In *Ciba Foundation Symposium 208—Characterizing Human Psychological Adaptations* (pp. 181–194). John Wiley & Sons, Ltd. https://doi.org/10.1002/9780470515372.ch10

Sotero, R. C., Bortel, A., Naaman, S., Mocanu, V. M., Kropf, P., Villeneuve, M. Y., & Shmuel, A. (2015). Laminar Distribution of Phase-Amplitude Coupling of Spontaneous Current Sources and Sinks. *Frontiers in Neuroscience*, *9*. https://www.frontiersin.org/article/10.3389/fnins.2015.00454

Spaak, E., Bonnefond, M., Maier, A., Leopold, D. A., & Jensen, O. (2012). Layer-Specific Entrainment of Gamma-Band Neural Activity by the Alpha Rhythm in Monkey Visual Cortex. *Current Biology*, *22*(24), 2313–2318. https://doi.org/10.1016/j.cub.2012.10.020

Szymanski, F. D., Garcia-Lazaro, J. A., & Schnupp, J. W. H. (2009). Current Source Density Profiles of Stimulus-Specific Adaptation in Rat Auditory Cortex. *Journal of Neurophysiology*, *102*(3), 1483–1490. https://doi.org/10.1152/jn.00240.2009

Thies, W., Kalko, E. K. V., & Schnitzler, H.-U. (1998). The roles of echolocation and olfaction in two Neotropical fruit-eating bats, Carollia perspicillata and C. castanea , feeding on Piper. *Behavioral Ecology and Sociobiology*, *42*(6), 397–409. https://doi.org/10.1007/s002650050454

Vianney-Rodrigues, P., Iancu, O. D., & Welsh, J. P. (2011). Gamma oscillations in the auditory cortex of awake rats. *The European Journal of Neuroscience*, *33*(1), 119–129. https://doi.org/10.1111/j.1460-9568.2010.07487.x

Virtanen, P., Gommers, R., Oliphant, T. E., Haberland, M., Reddy, T., Cournapeau, D., Burovski, E., Peterson, P., Weckesser, W., Bright, J., van der Walt, S. J., Brett, M., Wilson, J., Millman, K. J., Mayorov, N., Nelson, A. R. J., Jones, E., Kern, R., Larson, E., … Vázquez-Baeza, Y. (2020). SciPy 1.0: Fundamental algorithms for scientific computing in Python. *Nature Methods*, *17*(3), 261–272. https://doi.org/10.1038/s41592-019-0686-2

Wang, L., Saalmann, Y. B., Pinsk, M. A., Arcaro, M. J., & Kastner, S. (2012). Electrophysiological Low-Frequency Coherence and Cross-Frequency Coupling Contribute to BOLD Connectivity. *Neuron*, *76*(5), 1010–1020. https://doi.org/10.1016/j.neuron.2012.09.033

Weaver, K., Wander, J., Ko, A., Casimo, K., Grabowski, T., Ojemann, J., & Darvas, F. (2016). Directional patterns of cross frequency phase and amplitude coupling within the resting state mimic patterns of fMRI functional connectivity. *NeuroImage*, *128*. https://doi.org/10.1016/j.neuroimage.2015.12.043

Weineck, K., García-Rosales, F., & Hechavarría, J. C. (2020). Neural oscillations in the fronto-striatal network predict vocal output in bats. *PLOS BIOLOGY*, *18*(3), 29. https://doi.org/10.1371/journal. pbio.3000658

Winguth, S. D., & Winer, J. A. (1986). Corticocortical connections of cat primary auditory cortex (AI): Laminar organization and identification of supragranular neurons projecting to area AII. *The Journal of Comparative Neurology*, *248*(1), 36–56. https://doi.org/10.1002/cne.902480104

Xiao, Z., Martinez, E., Kulkarni, P. M., Zhang, Q., Hou, Q., Rosenberg, D., Talay, R., Shalot, L., Zhou, H., Wang, J., & Chen, Z. S. (2019). Cortical Pain Processing in the Rat Anterior Cingulate Cortex and Primary Somatosensory Cortex. *Frontiers in Cellular Neuroscience*, *13*. https://www.frontiersin.org/article/10.3389/fncel.2019.00165

Zion Golumbic, E. M., Ding, N., Bickel, S., Lakatos, P., Schevon, C. A., McKhann, G. M., Goodman, R. R., Emerson, R., Mehta, A. D., Simon, J. Z., Poeppel, D., & Schroeder, C. E. (2013). Mechanisms Underlying Selective Neuronal Tracking of Attended Speech at a "Cocktail Party." *Neuron*, *77*(5), 980–991. https://doi.org/10.1016/j.neuron.2012.12.037

Additional Information

Author contributions

Experiments were performed in the laboratories of the Leibniz-Institute for Neurobiology, Magdeburg (Germany), by KED and Institute for Cell Biology and Neuroscience, Goethe-University, Frankfurt/M (Germany) by FGR. Study was designed by KED, FGR, JCH, and MFKH. JCH and MFKH supervised the project. Data and statistical analysis were performed by KED and RK with input from FGR. KED prepared the figures and wrote the initial paper draft. Manuscript was edited by KED, FGR, RK, JCH, and MFKH. All authors reviewed the manuscript, approve of the final version, and agree to be accountable for all aspects of the work. All persons designated as authors qualify and all who qualify are listed as authors.

Data Availability

Scripts and data used in this research will be available from time of peer-reviewed publication at https://github.com/CortXplorer and https://figshare.com/ or on request.

Competing Interests

There were no conflicts of interest in this study.

Funding

This project was funded by the Leibniz Institute for Neurobiology (Special Project to MFKH), the Leibniz Association (WGL; Leibniz Postdoctoral Network, MFKH), and the German Research Council (DFG; Grant No. HE 7478/1-1 to JCH).

Acknowledgements

We would like to thank Dr. Michael Lippert and Alisa Vlasenko for their assistance with the head-fixation setup and the surgery for mice and Gisa Prange for help with the histology for bats.

Figures

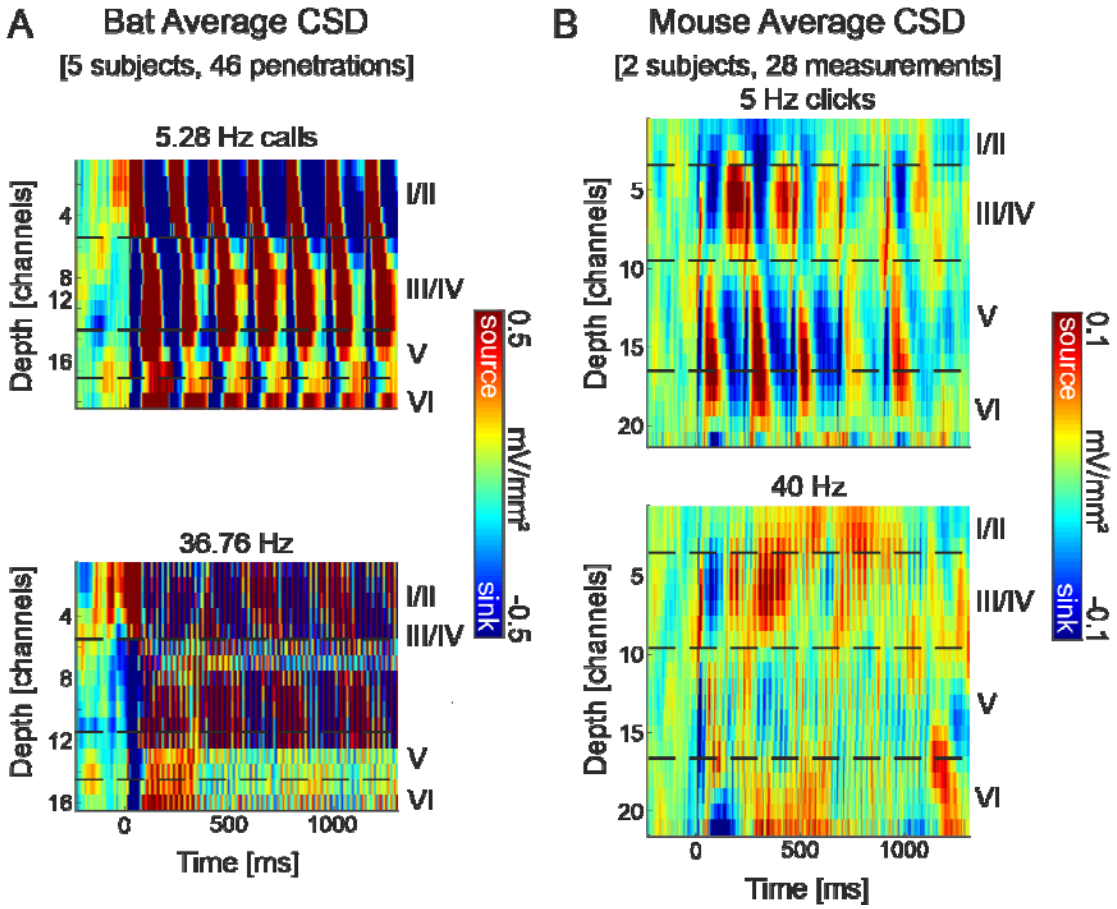

Figure 1 Grand average current-source density profiles. A: Seba's short-tailed bats (n = 5, 47 separate penetrations) grand averaged cortical response to a click-like distress call presented repetitively at 5.28 Hz (top) and 36.76 Hz (bottom). **B:** black 6 mice (n = 2, 28 measurements from 2 penetrations) grand averaged cortical response to a click train presented at 5 Hz (top) and 40 Hz (bottom). The CSD profiles show the pattern of temporal processing (ms) within the cortical depth (channels are 50 µm apart). Representative layer assignment is indicated with horizontal dashed lines. Current sinks (blue), represent areas of excitatory synaptic population activity, while current sources reflect balancing currents (cf. Happel et al., 2010). Note the different c-axis scales: with much stronger signal from bats; the different time scales: 2 s stimuli for bats and 1 s stimuli for mice; and the different depth scales: slightly thicker cortex for mice, ~20 channels or ~1 mm, than bats 16 channels or ~750 µm.

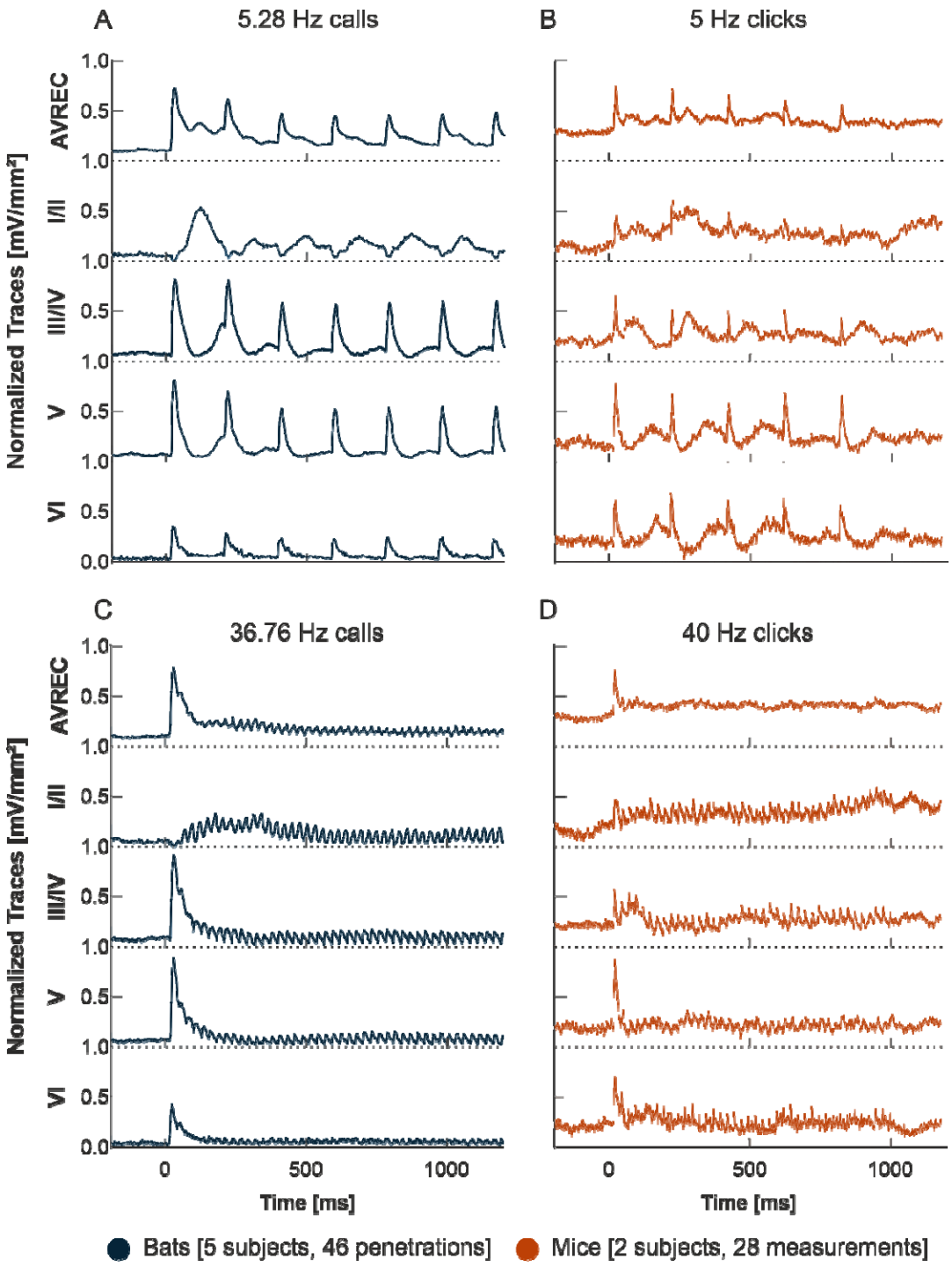

Figure 2 AVREC and layer traces. A, C: Bat averaged auditory cortex AVREC trace (top) and all layer traces (I/II, III/IV, V, VI in descending order), in response to 5.28 Hz or 36.76 Hz click-like distress calls (blue). **B, D:** Mouse averaged auditory cortex AVREC layer traces, in response to 5 Hz or 40 Hz click-trains (orange). Layer traces were calculated on sink activity only. Confidence intervals are shown in SEM. Traces were all normalized per measurement due to separate penetrations in bat group. Normalization was done according to the first detected peak of the AVREC at 2 Hz (not shown).

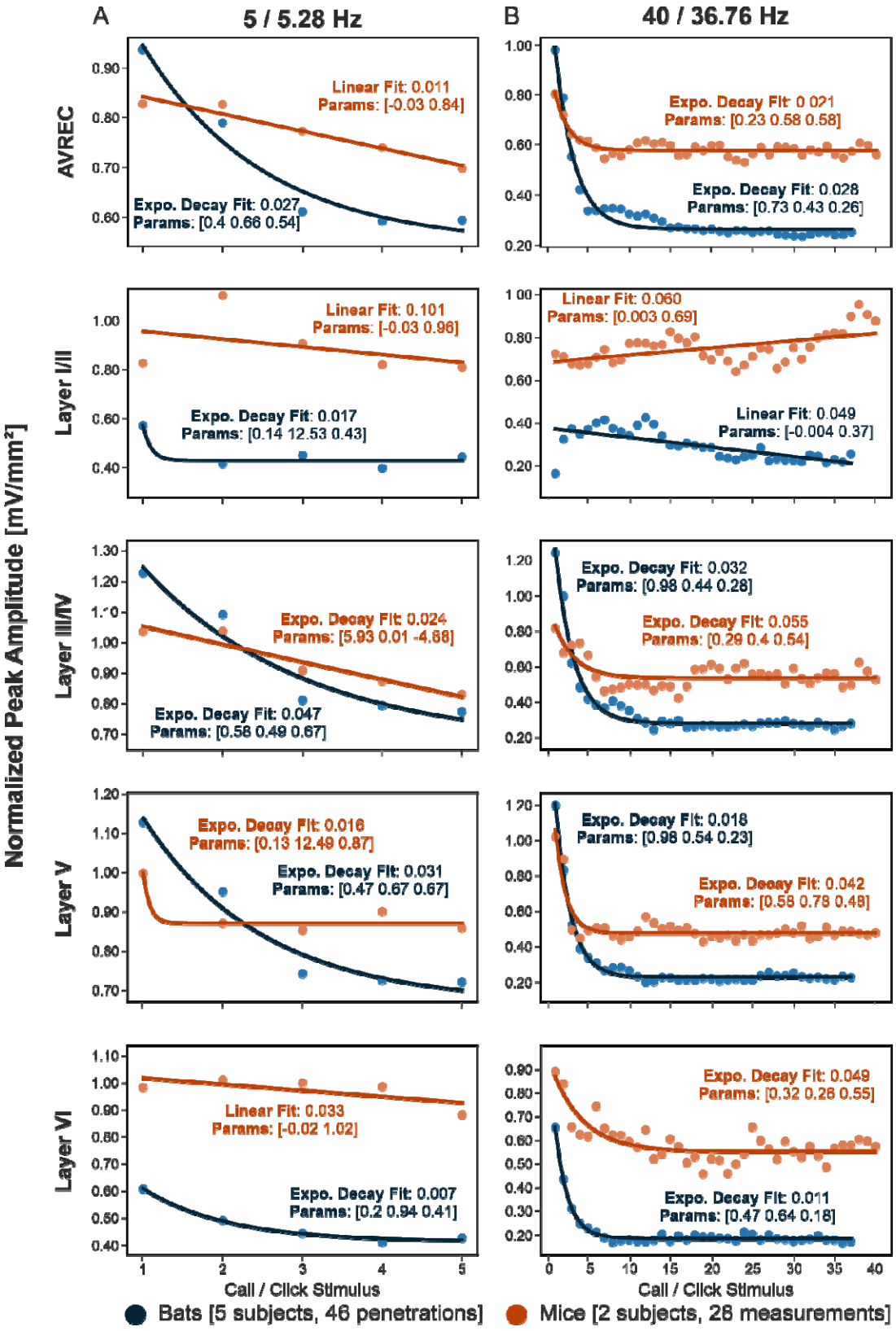

Figure 3 Model Fit Analysis. A: Bat (blue) and mouse (orange) group-averaged response peak amplitudes over consecutive stimulus repetition of 5 or 5.28 Hz with overlaid model fit. **B:** Bat and mouse group-averaged response peak amplitude over consecutive stimulus repetition of 40 or 36.76 Hz with overlaid model fit. The model selected, exponential or linear decay is overlaid, along with the fit value calculated by RMSE and the model parameters. The closer to zero that the model fit is, the better fit it is. For expo.: parameters are [dynamic range, rate of decay, offset]. For linear: [slope, intercept]

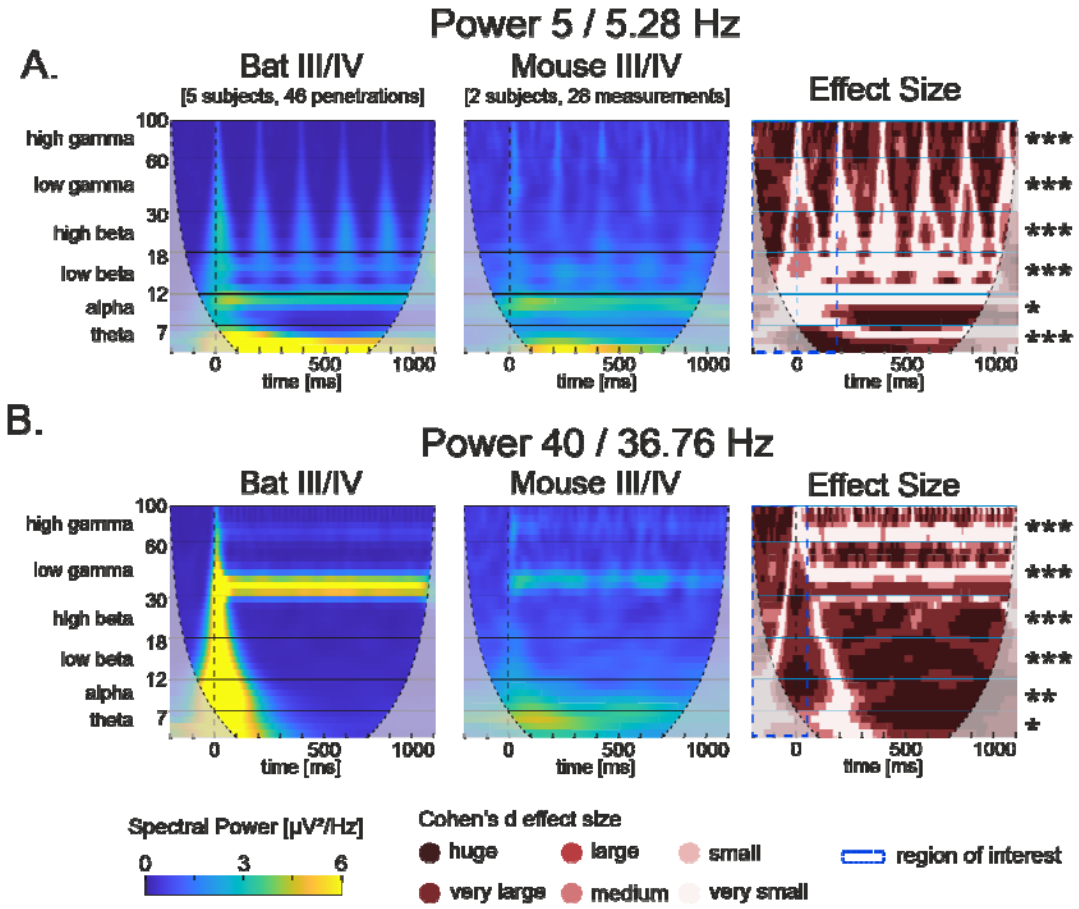

Figure 4 Power scalograms of continuous wavelet transform. A: bat (left) and mouse (middle) grand average power CWT profile of layer III/IV during ~5 Hz stimuli presentation. Cohen's d effect size results (right) are overlaid with ROIs (dashed blue box) from within which clustermass permutation analysis was run in each oscillatory band from -200 to 189 ms around the first stimulus presentation. Permutation results are shown as significance stars to the left. **B:** bat and mouse grand average power CWT profile, and effect size plot of layer III/IV during ~40 Hz stimuli presentation. Clustermass permutation ROI ran from -200 to 25 ms around the first stimulus presentation. Horizontal borders designated spectral frequency bins: theta: 4-7 Hz (skipping delta in this analysis), alpha: 8:12 Hz, beta low: 13:18 Hz, beta high: 19:30 Hz, gamma low: 31:60, gamma high: 61:30. *=p<0.05, **=p<0.01, ***=p<0.001

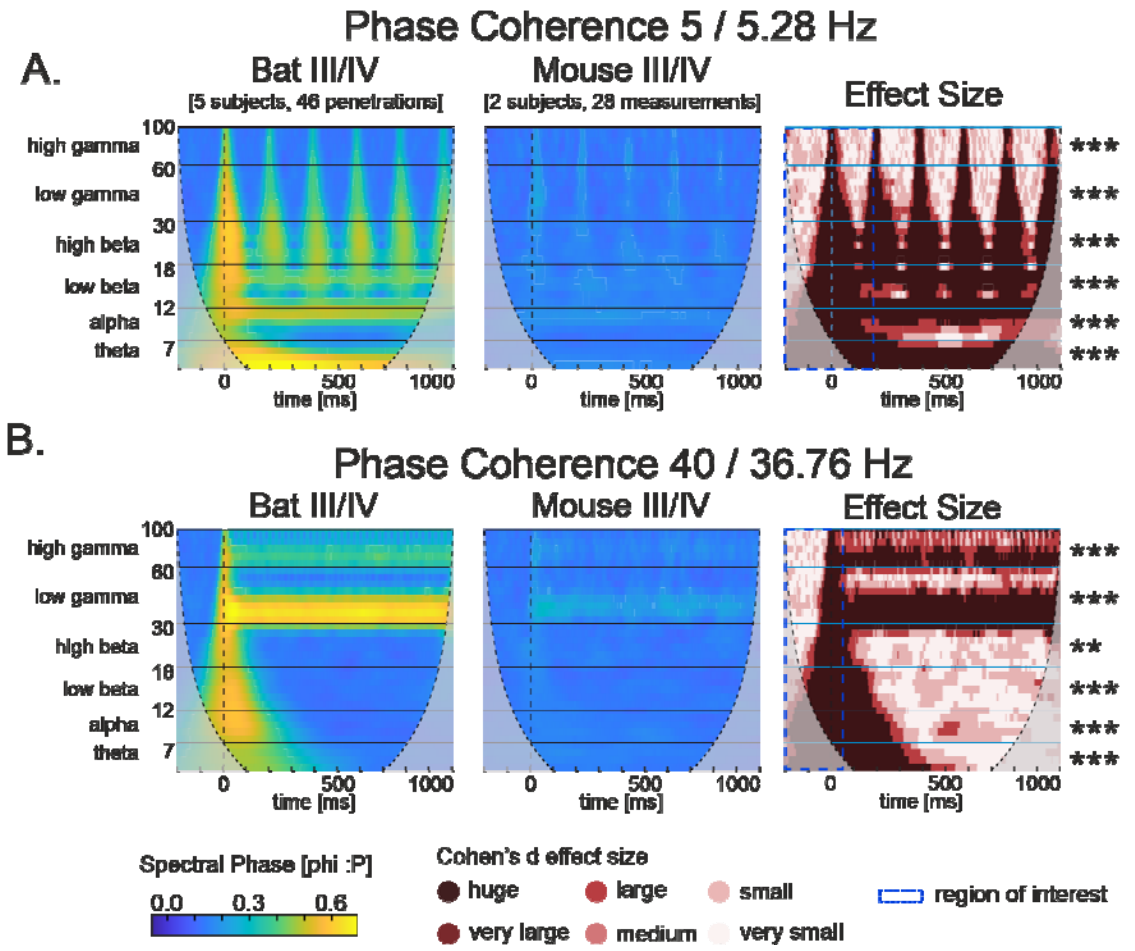

Figure 5 Phase coherence scalograms of continuous wavelet transform. A: bat (left) and mouse (middle) grand average power CWT profile of layer III/IV during ~5 Hz stimuli presentation. Cohen's d effect size results (right) are overlaid with ROIs (dashed blue box) from within which clustermass permutation analysis was run in each oscillatory band from -200 to 189 ms around the first stimulus presentation. Permutation results are shown as significance stars to the left. **B:** bat and mouse grand average power CWT profile, and effect size plot of layer III/IV during ~40 Hz stimuli presentation. Clustermass permutation ROI ran from -200 to 25 ms around the first stimulus presentation. Horizontal borders designated spectral frequency bins: theta: 4-7 Hz (skipping delta in this analysis), alpha: 8:12 Hz, beta low: 13:18 Hz, beta high: 19:30 Hz, gamma low: 31:60, gamma high: 61:30. *=p<0.05, **=p<0.01, ***=p<0.001

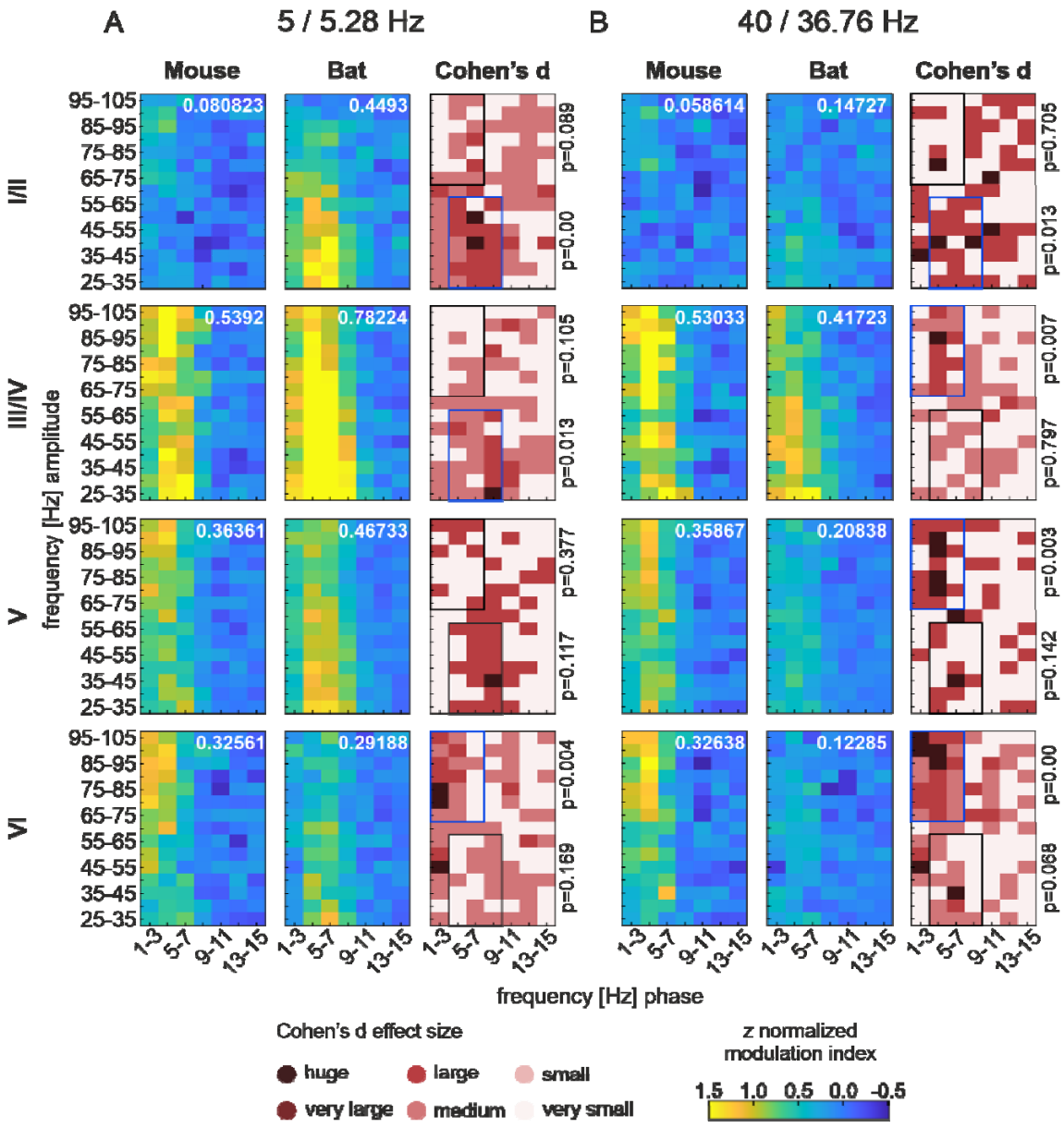

Figure 6 Phase amplitude coupling profiles over low and high freqyency. The PAC profiles, high frequency amplitude over low frequency phase, of mice and bats for each layer center channel (top to bottom) for **A:** ~5 Hz and **B:** ~40 Hz calculated from CSD signals. z-score normalized modulation index is represented in the color access, with higher zMI indicating better coupling. Point-wise Cohen's d effect size results shown in 3rd and 6th columns. Overlaid are ROI boxes where permutation clustermass analysis was calculated, blue if significant ($p<0.05$), black if not, with corresponding p values on the right. ROIs were chosen based on the areas of best coupling in each species and were kept consistant between all PAC analyses. Cohen's d 0.2-0.5 = small, 0.5-0.8 = medium, 0.8-1.2 = large, 1.2-2.0 = very large, >2.0 = huge.

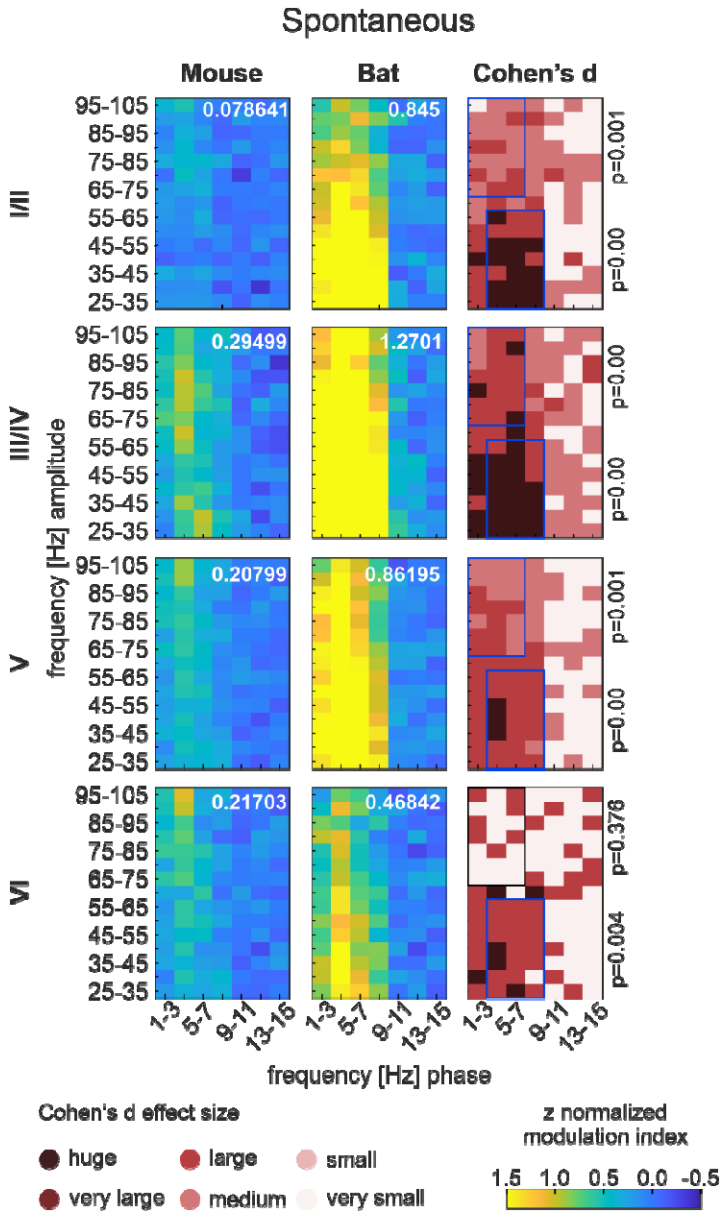

Figure 7 Phase amplitude coupling profiles from spontaneous activity. The PAC profiles, high frequency amplitude over low frequency phase, of mice and bats for each layer center channel (top to bottom) calculated from CSD signals. z-score normalized modulation index is represented in the color access, with higher zMI indicating better coupling. Point-wise Cohen's d effect size results shown in 3rd and 6th columns. Overlaid are ROI boxes where permutation clustermass analysis was calculated, blue if significant ($p<0.05$), black if not, with corresponding p values on the right. ROIs were chosen based on the areas of best coupling in each species and were kept consistant between all PAC analyses. Cohen's d 0.2-0.5 = small, 0.5-0.8 = medium, 0.8-1.2 = large, 1.2-2.0 = very large, >2.0 = huge.

Tables

		Normalized Power			Phase Coherence		
		p value	mean	std	p value	mean	std
~ 5 Hz	theta	**0.000**	116.776	201.918	**0.000**	110.574	369.175
	alpha	**0.028**	94.676	176.134	**0.000**	94.714	265.334
	beta low	**0.000**	83.174	127.432	**0.000**	89.876	211.257
	beta high	**0.000**	86.382	134.406	**0.000**	87.820	181.234
	gamma low	**0.000**	157.592	212.520	**0.000**	145.158	166.716
	gamma high	**0.000**	130.882	205.087	**0.000**	125.694	71.814
~ 40 Hz	theta	**0.014**	72.490	162.299	**0.000**	62.692	186.233
	alpha	**0.008**	53.774	125.424	**0.000**	40.466	131.779
	beta low	**0.000**	58.204	116.705	**0.000**	47.138	102.103
	beta high	**0.000**	50.516	86.014	**0.002**	52.118	86.863
	gamma low	**0.000**	88.592	113.666	**0.000**	85.342	86.573
	gamma high	**0.000**	69.468	96.232	**0.000**	74.210	51.314

Table 1 Between group CWT spectral band clustermass comparison. Corresponding to **Figure 4** &**Figure 5**. Bat vs Mouse region of interested comparisons of power and phase coherence scalograms for ~5 and ~40 Hz. ROI was the 200 ms before stimulus onset to 189 ms (for 5.28 Hz) or 25 ms (for 40 Hz) after stimulus onset in this condition for each spectral band. p value results and corresponding mean and std are shown. In bold are p values where significant above chance $p < 0.05$.

			CSD Signal PAC Perm		
Frequency	Layer	Region of Interest	p	mean	std
5 / 5.28 Hz	II	Delta / high gamma	0.089	2.548	2.057
		Theta / low gamma	**0.000**	2.300	2.925
	III/IV	Delta / high gamma	0.105	2.350	2.438
		Theta / low gamma	**0.013**	2.154	2.844
	V	Delta / high gamma	0.377	2.327	2.213
		Theta / low gamma	0.117	2.061	2.194
	VI	Delta / high gamma	**0.004**	2.413	2.047
		Theta / low gamma	0.169	2.070	1.989
40 / 36.75 Hz	II	Delta / high gamma	0.705	2.485	1.563
		Theta / low gamma	**0.013**	2.094	1.738
	III/IV	Delta / high gamma	**0.007**	2.213	2.107
		Theta / low gamma	0.797	2.106	2.094
	V	Delta / high gamma	**0.003**	2.401	1.790
		Theta / low gamma	0.142	1.951	1.544
	VI	Delta / high gamma	**0.000**	2.390	1.843
		Theta / low gamma	0.068	2.110	1.444
~	II	Delta / high gamma	**0.001**	2.445	2.766
		Theta / low gamma	**0.000**	2.090	3.596
	III/III/IV	Delta / high gamma	**0.000**	2.273	2.848
		Theta / low gamma	**0.000**	2.273	3.671
	V	Delta / high gamma	**0.001**	2.344	3.144
		Theta / low gamma	**0.000**	2.082	3.311
	VI	Delta / high gamma	0.376	2.364	2.201
		Theta / low gamma	**0.004**	2.042	2.260

Table 2 Between group PAC region of interest comparison Bat vs Mouse PAC profiles at delta-high gamma (1-7 Hz phase vs 65-105 Hz amp) and theta-low gamma (3-9 Hz phase vs 25-65 Hz amp) phase-amp couplings. Corresponding to **Figure 6** & **Figure 7.** Regions were chosen based on the PAC profiles and not exact spectral frequency bins. Comparisons were done with the same regions across all layers and stimulus conditions. p value results and corresponding mean and std are shown. In bold are p values where significant above chance $p < 0.05$.

Supplemental Figures

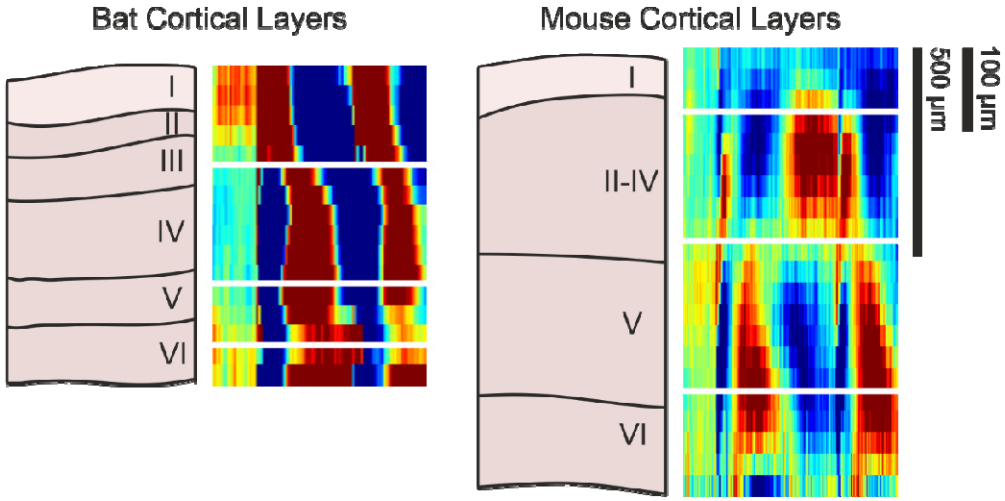

Supp Figure 1 Anatomical comparison; A representation of an A1 columnal section and lines denoting rough layer boundaries were generated based on figures from García-Rosales et al. (2019) for Seba's short-tailed bat A1 laminar anatomy and from Chang & Kawai (2018) for black 6 mouse A1 laminar anatomy. These are set next to appropriately and relatively sized group average CSD profiles (Figure 1; 1 mm for mice and 750 µm for bats) to show representative layer designations in comparison with these references.

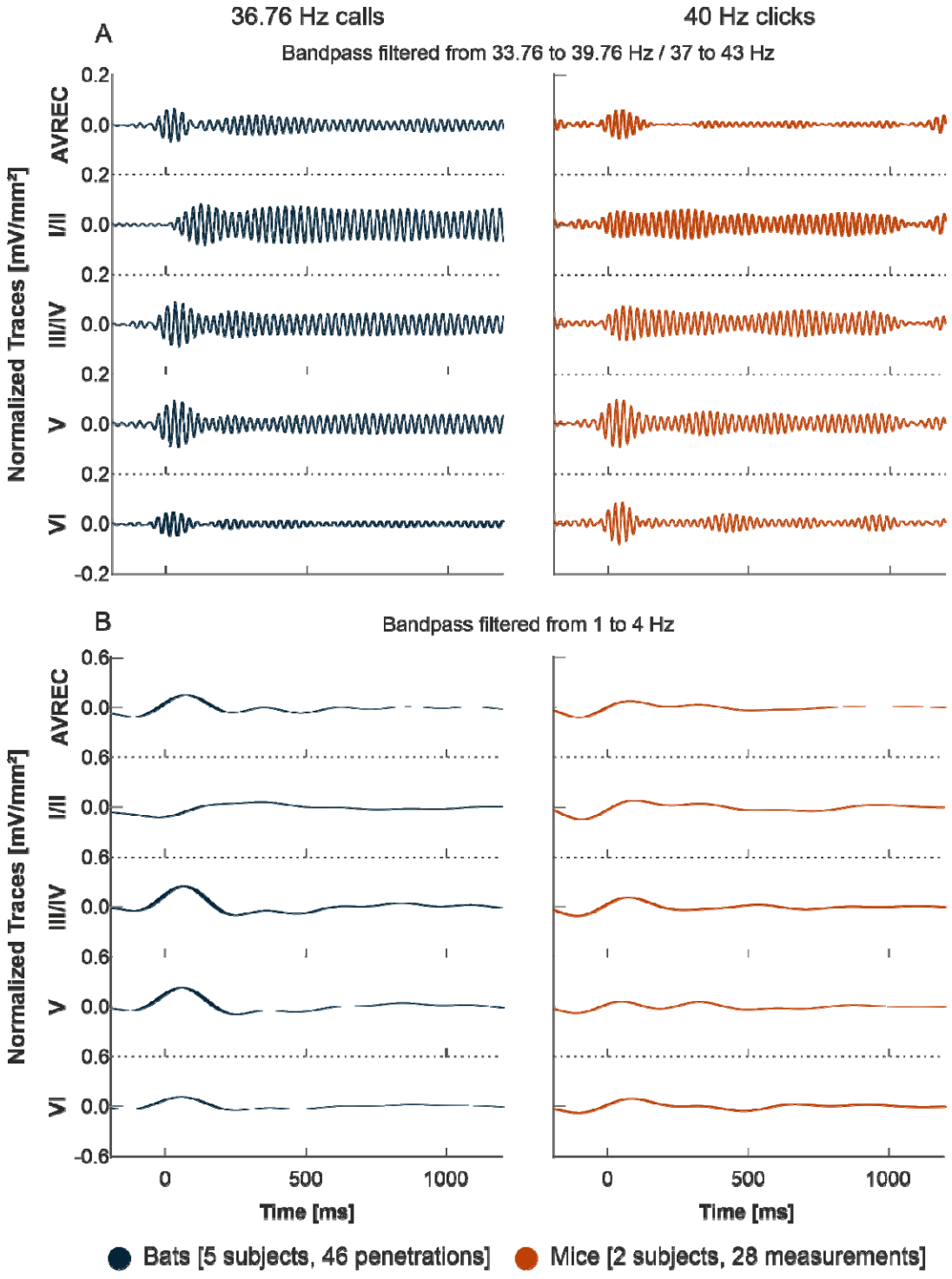

Supp Figure 2 AVREC and layer traces bandpass filtered. A: Bat averaged auditory cortex AVREC trace (top) and all layer traces (I/II, III/IV, V, VI in descending order), in response to 36.76 Hz click-like distress calls (blue) bandpass filtered 3 Hz above and below presentation frequency and **C:** bandpass filtered from 1 to 4 Hz. **B:** Mouse averaged auditory cortex AVREC and layer traces, in response to 40 Hz click-trains (orange)) bandpass filtered 3 Hz above and below presentation frequency and **D:** bandpass filtered from 1 to 4 Hz. Layer traces were calculated on sink activity only. Confidence intervals are shown in SEM. Traces were all normalized per measurement due to separate penetrations in bat group. Normalization was done before filtering according to the first detected peak of the AVREC at 2 Hz (not shown).

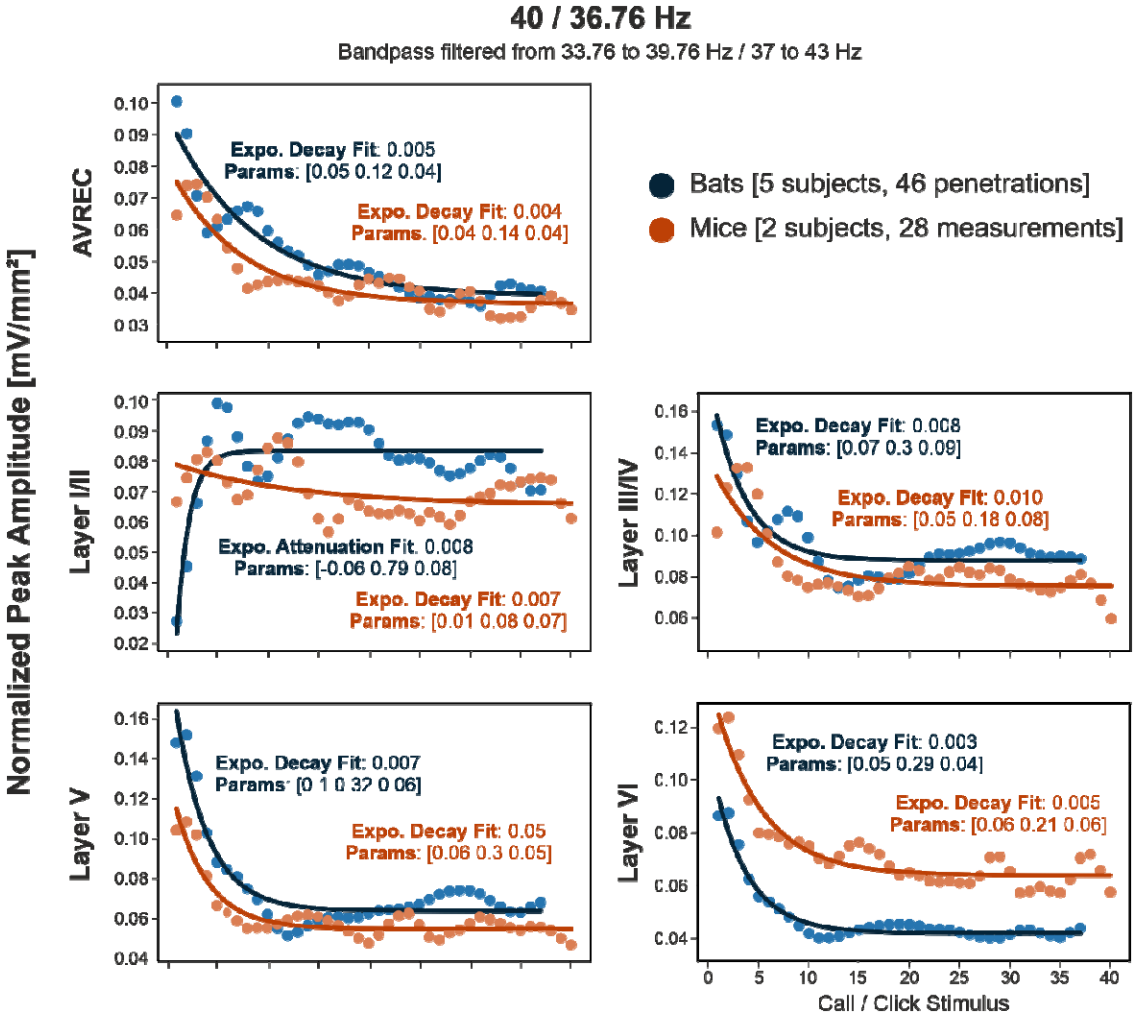

Supp Figure 3 Model Fit Analysis bandpass filtered. Bandpass filtered +/- 3 Hz around the presentation frequency, bat (blue) and mouse (orange) group-averaged response peak amplitudes over consecutive stimulus repetition of 40 or 36.76 Hz with overlaid model fit. The model selected, exponential or linear decay is overlaid, along with the fit value calculated by RMSE and the model parameters. The closer to zero that the model fit is, the better fit it is. For expo.: parameters are [dynamic range, rate of decay, offset]. For linear: [NA]